Journal of Natural Gas Science and Engineering 96 (2021) 104248

Contents lists available at ScienceDirect

Journal of Natural Gas Science and Engineering

journal homepage: www.elsevier.com/locate/jngse

Pore-scale heterogeneity of tight gas sandstone: Origins and impacts

Juncheng Qiao [a,b,c,**], Jianhui Zeng [a,b,*], Jianchao Cai [a,b], Shu Jiang [c], Ting An [d], Enzhao Xiao [e], Yongchao Zhang [f], Xiao Feng [a,b], Guangqing Yang [a,b]

[a] State Key Laboratory of Petroleum Resources and Prospecting, China University of Petroleum, Beijing, 102249, PR China
[b] College of Geosciences, China University of Petroleum, Beijing, 102249, PR China
[c] Energy & Geosciences Institute and Department of Chemical Engineering, University of Utah, Utah 84108, United States
[d] Fengcheng Oilfield Operation District, Xinjiang Oilfield Company, CNPC, Keramay, 834000, PR China
[e] Key Laboratory for Polar Science, MNR, Polar Research Institute of China, Shanghai, 200136, PR China
[f] The Key Laboratory of Gas Hydrate, Ministry of Natural Resources, Institute of Marine Geology, Qingdao, 266071, PR China

ARTICLE INFO

Keywords:
Tight gas sandstone
Pore-scale heterogeneity
Fractal
Geological controlling factors
Fluid accessibility
Permeability

ABSTRACT

Pore-scale heterogeneity attracts attentions in tight gas sandstone as it strongly affects the hydrocarbon deliverability. However, its controls and origins remain obscure owing to the intricate physical and chemical interplays in tight sandstone. Moreover, its effects on fluid propagation are rarely discussed. This paper aims to investigate controls and origins of pore-scale heterogeneity and its impacts on fluid accessibility by integrated experiments incorporating fractal, petrologic, and fluid accessibility analyses. The dominant tri-fractal structures with wide fractal dimension ranges suggest intense pore-scale heterogeneities of tight sandstone. Pore-scale heterogeneities originate from pore attributes. The heterogeneities of large-sized and medium-sized pores are mainly determined by quantities of macropore and mesopore, respectively, while that of small-sized pore is dominated by the size of small-micro pore and content of intercrystalline pore. The system heterogeneity is a coupled expression of the morphology, geometry, and genesis of different-sized pores. Mineralogy and petrology exert complex influences. The rigid grain is generally favorable for pore-scale homogeneities, but carbonate is on opposite. Greater clay content reduces the heterogeneity of small-sized pore, increases that of medium-sized pore, but increases that of large-sized pore before 5% and then reduces it. Greater grain size and better sorting bring reductions to the heterogeneity of small-sized pore but increases to those of medium- and large-sized pores. The heterogeneities of large-sized pore, medium-sized pore, and pore system are susceptible to pore fillings, while that of small-sized pore is susceptible to matrix grains. The fluid accessibility differences in the medium- and large-sized pores, affected by the pore-scale heterogeneity variations, are responsible for system fluid mobility distinctions. The influences of heterogeneity on fluid accessibility increase with pore size but accessibility of small-sized pore is barely not affected by its heterogeneity owing to clay hydrophillia. The Coates model is improved by calibrating fluid accessibility and considering system heterogeneity.

1. Introduction

Tight sandstone, an unconventional reservoir with low porosity (<10%) and ultralow permeability (absolute permeability $<1 \times 10^{-3}$ μm^3), exhibits great hydrocarbon and geothermal potentials (Holditch, 2006; Rezaee et al., 2012; Zou et al., 2012). The traits of microscopic structures govern the physical and chemical interplays in the natural porous media, especially the fluid transportation and hydrocarbon deliverability (Katz and Thompson, 1986; Tiab and Donaldson, 2004; Dullien, 2012; Bear, 2013; Xiao et al., 2017; Qiao et al., 2020a). Characterizing the extreme intricate pore structure emerges as a long-term focus in tight sandstone (Soeder, 1984; Desbois et al., 2011; Clarkson et al., 2012a, 2013; Wilson et al., 2014; Huang et al., 2018; Lai et al., 2018a, 2018b). Although a plenty of parameters have been proposed to describe the average pore attributes, including the porosity, pore size distribution, volume, surface area, and etc. (Peng et al., 2011), challenges still present in the description of microscopic heterogeneity owing to the failures of traditional Euclidean geometry (Soeder and

* Corresponding author. State Key Laboratory of Petroleum Resources and Prospecting, China University of Petroleum, Beijing, 102249, PR China.
** Corresponding author. State Key Laboratory of Petroleum Resources and Prospecting, China University of Petroleum, Beijing, 102249, PR China.
E-mail addresses: Juncheng.Qiao@cup.edu.cn (J. Qiao), zengjh@cup.edu.cn (J. Zeng).

https://doi.org/10.1016/j.jngse.2021.104248
Received 28 March 2021; Received in revised form 21 August 2021; Accepted 13 September 2021
Available online 23 September 2021

Chowdiah, 1990; Tsakiroglou and Payatakes, 2000; Radlinski et al., 2004; Clarkson et al., 2012b; Wang et al., 2012; Fu et al., 2017).

Fractal dimensions have been accepted to probe the geometry of irregular objects with self-similarity (Mandelbrot, 1975; Mandelbrot et al., 1984). It has been introduced to the hydrocarbon and geothermal reservoirs, such as coal, shale, granite, and tight sandstone (Krohn and Thompson, 1986; Friesen and Mikula, 1987; Yang et al., 2014; Song et al., 2018) due to the fractal natures of pores in the natural porous reservoirs (Katz and Thompson, 1985; Krohn and Thompson, 1986). Pore fractal dimensions can be obtained by various techniques, including the imaging-based analysis (Hansen and Skjeltorp, 1988; Krohn, 1988; Peyton et al., 1994; Pan et al., 2016; Rahner et al., 2018; Xia et al., 2019), fluid-invasion methods (Angulo et al., 1992; Li and Horne, 2006; Li, 2010; Lai and Wang, 2015), radiation techniques (Bale and Schmidt, 1984; Bahadur et al., 2014; Daigle et al., 2014a, 2014b; Zhou et al., 2016; Sun et al., 2017; Zheng et al., 2018), and gas absorption analyses (Yao et al., 2008; Liu et al., 2015; Yang et al., 2016; Yuan and Rezaee, 2019). However, the determination of fractal dimension of tight sandstone depends on the techniques employed and is limited by their deficiencies in the measuring the overall pore structures (Cai et al., 2015; Ge et al., 2015; Li et al., 2017). Recently, Wu et al. (2019) have reported that nuclear magnetic resonance (NMR) is a promising tool in the fractal analyses of tight sandstone by comparing the mercury intrusion porosimetry (MIP), NMR, and X-ray computed tomography (X-CT) techniques.

Despite the various discussions on the fractal dimension measurements, the controls and origins of fractal pores in natural porous media remain obscure. The geometry, complexity, morphology of pores in sedimentary reservoirs are the expressions of the coupled effects of sedimentation and diagenesis. It suggests that the pore fractal natures originate from the physical and chemical interactions between mineral, fluid, and mineral-fluid (Giles and Marshall, 1986; Bjørlykke et al., 1989; Katsube and Williamson, 1994; Zhu et al., 2008; Lai et al., 2015; Dou et al., 2018; Qiao et al., 2020b). Investigation of the origins and controls of multi-fractals becomes the critical path to understand the pore-scale heterogeneity of reservoir rock. Recent publications in shale and coal have noticed the correlations between the fractal dimensions and TOC, Ro, volatile content, coal macerals, and clay mineral content (Liu et al., 2015; Jiang et al., 2016). However, the origins and controls of the multi-fractal pores in tight sandstone remain unclear as more factors should be taken into account owing to the complicated petrology, mineralogy, and fluid-mineralogy interactions of tight sandstone (Ge et al., 2015; Liu et al., 2018).

The macroscopic fluid propagation is governed by the frameworks of microscopic pore structure (Arshadi et al., 2018; Liu et al., 2020; Wang et al., 2021). Relating the fluid transportation properties of reservoir rocks to their pore structures has been brought to forefront, especially in tight sandstone and shale (Sahimi, 1993; Blunt, 1998; Aghaei and Piri, 2015). Currently, the cross-properties between the pore geometry attributes (e.g. hydraulic radius, critical channel diameter, average pore-throat size, and connectivity) and fluid transportation parameters (permeability, fluid saturation, and fluid mobility) have been reported (Bourbie and Zinszner, 1985; Gallegos et al., 1987; Arns et al., 2001, 2005; Daigle and Dugan, 2009; Daigle and Johnson, 2016). The impacts of pore-scale heterogeneity on fluid flow capacity attract research interest since Pape et al. (1999) and Xia et al. (2019) noticed the correlations between the fractal dimension and permeability. However, the understanding for them is still superficial.

Logically integrated investigation, including NMR, X-ray CT, casting thin section (CTS), scanning electron microscope (SEM) and grain analysis, incorporating fractal theory, petrology analysis, and fluid accessibility evaluation, gives out the major objects of this paper: to describe the pore-scale heterogeneity of tight gas sandstone in quantitative, to analyze its origins and controls in terms of petrology, mineralogy, and pore microstructure, and to probe its impacts on the fluid accessibility.

2. Sample information and methods

2.1. Sample information

The Shanxi Formation in the Ordos basin is characterized by transitional sediments with interbedded coal measures, mudstone, and siltstone layers (Tang et al., 2012; Zhao et al., 2014), of which the tight sandstone members exhibit great natural gas potentials (Yang et al., 2008, 2012). The sampling was conducted on the major reservoir rocks, lacustrine lithic fine to medium sandstones, in the formation (Xiao et al., 2005; Qiao et al., 2020c).

Firstly, fifty cylindrical plugs with lengths and diameters of approximately 5.00 cm and 2.50 cm, respectively, were drilled from the fresh cores. They included the fine, medium, and coarse lithic sandstones and covered the majority of the types of the reservoir rocks. The samples underwent an impurity and residual hydrocarbon removal, followed by a 48-h drying under a temperature of 120 °C before the tests. The porosity and permeability were measured by a CMS-300 core instrument in the State Key Laboratory of China University of Petroleum -Beijing (CUPB), of which the gas expansion and pressure transient (confining pressure of ~1.5 MPa) were employed to probe the helium porosity and permeability (Klienkenberg-corrected) under the environment temperature of 20 °C, respectively. After the measurements, a sample selection that covered the major porosity and permeability ranges of tight gas sandstone in the formation was done with reasonable intervals in order to guarantee the sampling representativeness and provide a solid data basis. Thirteen representative samples were chosen from the fifty specimens (Table 1).

2.2. Experiments

2.2.1. Experimental process

A logically integrated experimental process was performed on the thirteen representative samples. The procedure obeyed the principles that all of the tests were conducted on same specimens and non-destructive analyses were priority to the destructive experiments in order to eliminate the sampling differences and to avoid destructive effects, respectively. Therefore, the X-ray CT analysis was firstly performed on the pretreated samples, followed by the NMR tests involving the saturated and centrifuged measurements. After that, thin slices were cut from the plugs and prepared for the CTS and SEM observations. In the last, parts of the samples were mechanically dispersed for the grain size measurement. The details of each experiments involved will be introduced in the following section.

2.2.2. Experiments

The X-ray CT was performed on core plugs using the Zeiss Xradia Versa-510 Micro-CT instrument in the State Key Laboratory of CUPB. The scanning set a voltage of 100 Kv, a current of 90 μA, an exposure time of 2.0 s, and a resolution of 3.0 μm under an environment temperature of 20 °C and a humidity of 40–50%. It guaranteed a good penetration with transmitted photon numbers greater than 6000 and high-quality imaging with few noises. Grayscale image reconstruction was done on the original scanning data employing the Zeiss Reconstruction Software, of which hundreds of grayscale hexadecimal tomography images were acquired. Filtering, segmentation, pore separation, and pore network modelling (PNM) aiming to obtain the detailed information of the pore system were performed on the tomography images using FEI AVIZO 9.0.1. The processing principle, methodology, and flow have been thoroughly explained by Qiao et al. (2020c) and Dong and Blunt (2009).

NMR analysis was then conducted on the same specimens by employing the Recore-04 low-field NMR spectrometer with a resonance frequency of 2.38 MHz. The test had an echo time of 0.15 ms, a waiting time of 2 s, scanning times of 32, and an echo number of 5000. The first-time NMR measurements were conducted after the samples were

Table 1
Petrology and texture of the samples.

Sample	Depth	Porosity (%)	Permeability (mD)	average grain size (μm)	Sorting	Roundness	Sorting coefficient	Skewness
1	2642.58	3.222	0.312	84.79	good	medium	2.58	1.59
4	2706.00	7.549	0.670	171.94	medium	medium	2.19	1.93
5	2686.80	5.777	0.187	152.83	poor	medium	1.99	2.08
6	2578.53	13.044	0.820	121.58	good	good	2.00	1.98
8	2751.60	1.050	0.041	101.15	poor	poor	2.06	1.97
11	2408.97	1.336	0.415	92.14	poor	medium	2.35	1.80
12	2433.86	4.487	1.966	196.78	poor	medium	2.39	1.78
15	2584.00	4.645	0.343	167.24	medium	medium	2.19	1.92
20	2685.60	5.049	0.669	116.62	good	good	2.13	1.92
23	2575.45	7.489	0.557	101.53	medium	medium	2.39	1.65
25	2347.30	0.106	0.012	119.08	poor	good	2.34	1.82
26	2768.20	7.048	0.135	136.79	medium	medium	2.14	1.92
27	2786.65	2.250	0.119	141.61	medium	poor	2.10	1.97

vacuumized and saturated with brine solution for 48 h. The experiments were performed at a temperature of 20 °C, an atmospheric pressure, and an environment humidity of ~40%, following the testing standard of China SY/T 6490–2014. The second-time NMR measurements were performed after the saturated samples had been centrifuged at a centrifugal force of 300 psi for 1 h in the high-speed centrifuge (temperature of 20 °C and environment humidity of ~40%). Carr-Purcell-Meiboom-Gill sequence was adopted to obtain the relaxation time of the saturated and centrifuged specimens, of which the saturation and centrifugation T_2 spectrums were acquired.

The brine solution was removed from the sample after two-times NMR tests. Then the samples underwent a second-time 48 h drying at a temperature of 120 °C. Thin slices were cut from the dried samples, which were grinded to thin sections with thickness of ~0.3 mm and thin slices with thickness of ~1 mm, respectively. Thin section impregnated by blue resin was observed by a FEI polarized microscope. Dozens of micrographs were collected, in which the mineral contents and pore types and constituents were estimated by point counting. SEM was performed on the polished and golden-coated thin slices using an FEI Quanta 200 scanning electron microscope with highest resolution of 1 nm. A series of images were collected from the secondary electronic imaging to observe the pore morphology and interstitial fillings. Grain size analysis followed the observation, parts of the dried samples were mechanically dispersed in a quartz mortar after they had been soaked in the 10% HCl solution for 48 h under normal temperature and pressure. A Malvern 3000 laser diffraction instrument was used in the measurement, of which the grain sizes were obtained on the basis of the mathematical relationships between the intensity of the laser diffraction and grain size.

2.2.3. Application of fractal theory

According to the fractal principle, the number of pores with radii greater than r- $N(r)$ are positively correlated with pore radii, which can be described as $N(r) \propto r^{-D_f}$, where the D_f is the fractal dimension (Ge et al., 2016; Li et al., 2017). The fractal relationship can be described as $P(r) = Cr^{-D_f-1}$ since the density function of pore radii $P(r)$ has been introduced (Zhang et al., 2007). Accordingly, the fractal correlation between the cumulative volume fraction of pores less than r-S_V and r can be expressed as $S_V = \left(\frac{r}{r_{max}}\right)^{3-D_f}$ (Daigle et al., 2014a, 2014b; Zhao et al., 2017; Zhang et al., 2020). On the basis of the relationship between r and T_2 (Coates et al., 1991; Daigle et al., 2014a; Dillinger and Esteban, 2014), the fractal relationship can be converted to $S_V = \left(\frac{T_2}{T_{2max}}\right)^{3-D_f}$, which can be transformed to Eq. (1) by taking logarithm on both sides. Therefore, the fractal dimensions can be derived by employing the NMR T_2 spectrum, of which the D_f of the pores in the certain ranges of sizes can be obtained by the slope k of the linear segments on the double logarithmic plots of S_V against T_2 and equals to 3-k (Lai et al., 2018).

$$Log(S_V) = (3 - D_f)LogT_2 - (3 - D_f)LogT_{2max} \quad (1)$$

3. Results

3.1. Reservoir quality, petrology, and mineralogy

The porosities and permeability of the thirteen selected samples are in the range 0.1–13.1% (avg. 4.85%) and 0.012–1.966 mD (avg. 0.480 mD), respectively. They are poorly correlated. The measurements confirm the poor reservoir qualities of Permian Shanxi tight sandstone. The variations of porosity and permeability in reasonable intervals among the thirteen samples guarantee their representativeness in the study area (Table 1).

Complicated grain textures are identified in the lithic quartz and lithic tight sandstone samples, with medium to good rounding, poor to good sorting, and fine to coarse grain sizes (Fig. 1 A-D, Fig. 2 A, B). The samples share similar bimodal grain size distributions with left and right peaks spanning the range 1–2.25 ϕ and 5–6 ϕ, respectively, and similar cumulative grain size distributions (Fig. 2 A, B, Table 1). However, the wide ranges of medium grain sizes between 84.79 and 196.78 μm supported the observation. According to the Folk standard (Boggs and Boggs, 2009), the calculated sorting coefficients are in the range 2.00–2.58 (avg. 2.21) and skewness is in the range 1.59–2.08 (avg. 1.87) (Table 1), also agreeing with the observations. The varied textures of the thirteen samples confirm the representativeness of the sampling.

Point counting estimation on the CTS micrographs gives out the mineralogy of the samples (Table 2), which are dominated by quartz and rock fragments, followed by clay and carbonate. Feldspar is volumetrically minor owing to the extensive dissolution resulted by organic acid and CO_2 fluid injection during the period of organics maturity. The quartz content is in the range 48.55–76.25% (avg. 66.84%), showing positive correlations with porosity and permeability. The rock fragment content ranges from 10.25 to 36.48% with an average of 21.33%, negatively correlated to the porosity and permeability (Fig. 2 C and D). The clay content is in the range 0.8–7.25%, exhibiting poor relationships with petrophysical properties. The carbonate and feldspar contents are minor, which are in the range 1–6.42% and 1–6.16%, respectively. The carbonate content exhibits negative correlations with the porosity and permeability (Fig. 2 C, D). The varied contents of different minerals suggest the differences in the mineralogy of the samples.

3.2. Pore type, morphology, and geometry

Five pore types are identified in the samples, including the primary intergranular pores (P-interG), dissolution intergranular pores (D-interG), dissolution intragranular pores (D-intraG), intercrystalline pores (InterC), and micro fractures (MF) (Fig. 1A–D). The P-interGs commonly show regular shapes with long dimensions ranging from dozens to hundreds of microns (Fig. 1 A). The D-interGs are spaces

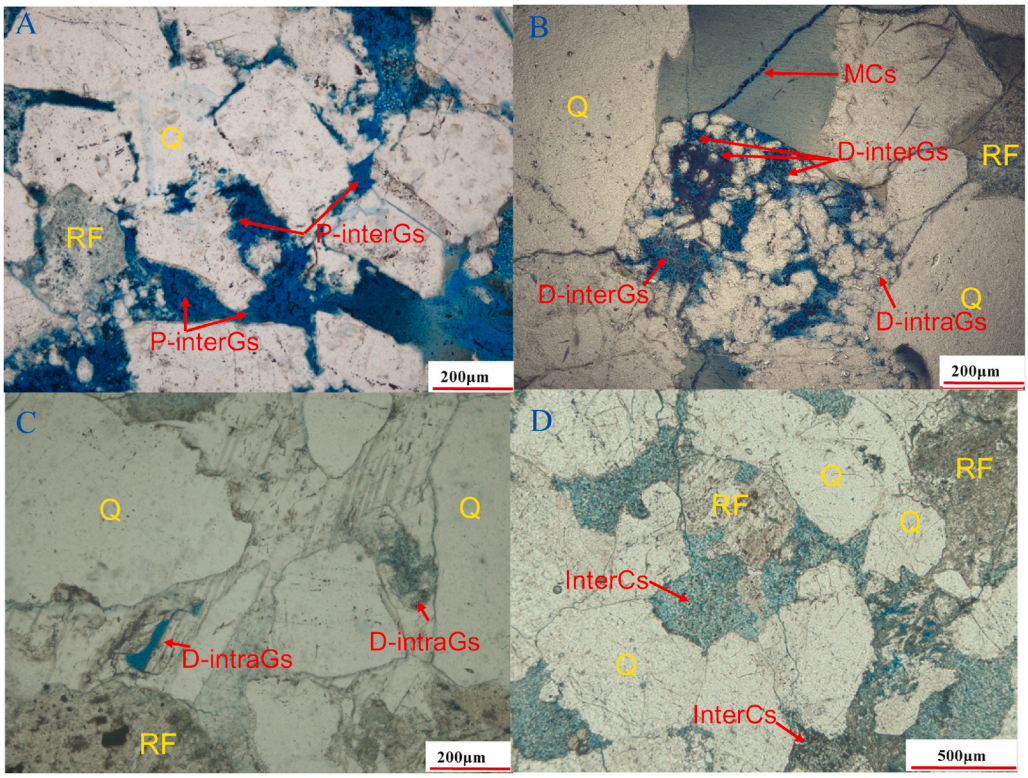

Fig. 1. Petrology and pore types of tight gas sandstone observed by CTS. (A) Fine-grained lithic quartz sandstone with plane viewed porosity dominated by primary intergranular pores. (B) Medium-grained lithic quartz sandstone with plane-viewed porosity dominated by dissolution intergranular pores and micro fractures. (C) Medium-grained lithic quartz sandstone with plane-viewed porosity dominated by dissolution intragranular pores. (D) Medium-grained lithic sandstone with plane-viewed porosity dominated by intercrystalline pores. (Note that P-interGs, D-interGs, D-intraGs, InterCs, and MCs separately refer to primary intergranular pores, dissolution intergranular pores, dissolution intragranular pores, intercrystalline pores, and micro fractures. Q and RF refers to quartz and rock fragment, respectively).

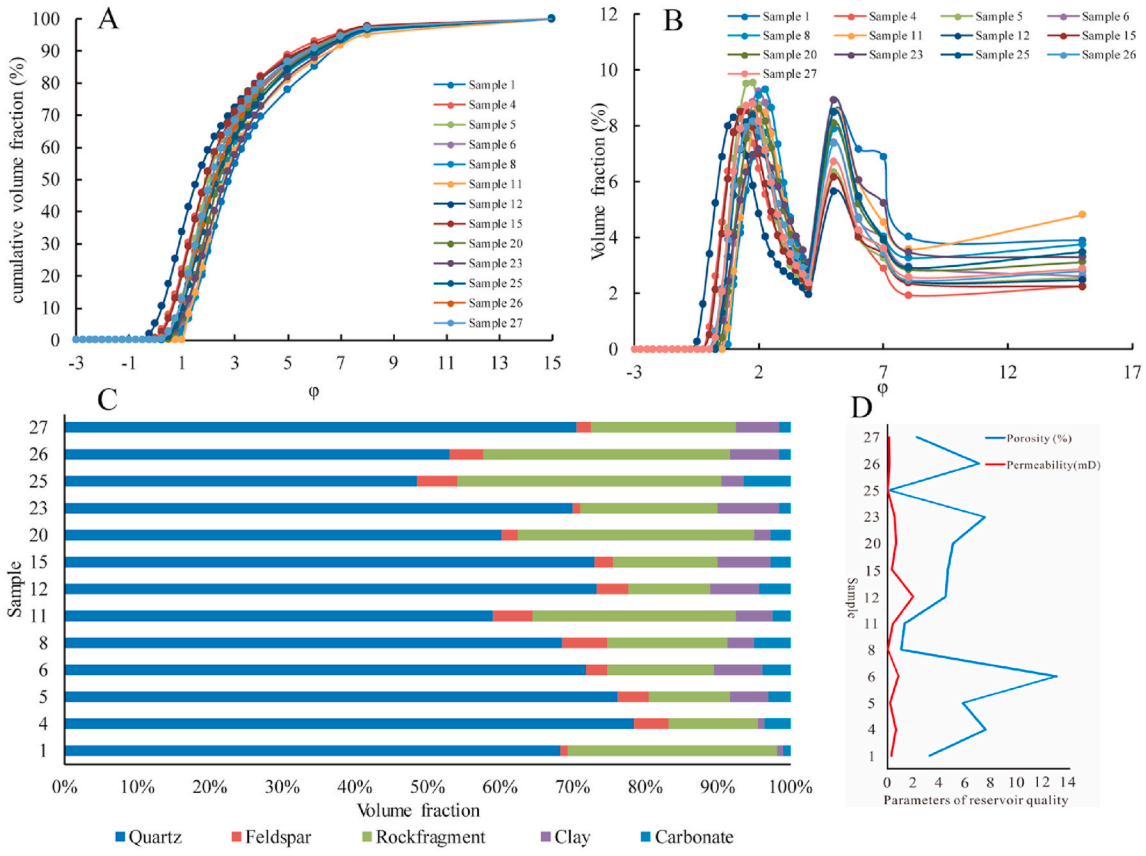

Fig. 2. Grain size, mineralogy, and reservoir quality of tight gas sandstone. (A) The cumulative grain size distributions, (B) normalized grain size distributions, (C) histograms for the mineral constitutes, and (D) porosity and permeability plots.

Table 2
Mineralogy of the tight sandstone samples.

Sample	Quartz (%)	Feldspar (%)	Rock fragment (%)	Clay (%)	Carbonate (%)
1	68.30	1.00	28.90	0.80	1.00
4	76.50	4.75	10.25	8.00	0.50
5	76.25	4.16	11.26	5.33	3.00
6	71.80	3.00	14.60	6.80	3.80
8	68.60	6.16	16.60	3.60	5.04
11	59.00	5.50	28.00	5.00	2.50
12	73.30	4.33	11.30	6.74	4.33
15	73.00	2.50	14.50	7.25	2.75
20	60.16	2.33	32.50	2.21	2.80
23	70.00	1.0	19.00	8.50	1.50
25	48.55	5.55	36.48	3.00	6.42
26	53.00	4.75	34.00	6.75	1.50
27	70.50	2.00	20.00	6.00	1.50

generated from the dissolution along the edges between the intergranular spaces and mineral particles, having similar long dimensions with P-interGs but irregular shapes (Fig. 1 B). The two types of pores can be classified as intergranular pores in location (Fig. 3). The D-intraGs originated from the dissolution inside the particles show smaller long dimensions ranging from several microns to dozens of microns, exhibiting zigzag pore shapes and irregular orientations (Fig. 1 B and C). The InterCs are tiny spaces between the clay aggregates (e.g. kaolinite, illite, and chlorite) with widths of hundreds of nanometers, whose appearances are determined by the aggregate arrangements (Fig. 1 D). The D-intraGs and InterCs belong to intragranular pores in location (Fig. 3). The MFs are slit pores with tiny widths of several microns and lengths of hundreds of microns, which may run through the grains and connected the pores. Four kinds of pore systems are identified employing the pore system classification criterion proposed by Qiao et al. (2020b) (Fig. 3, Table 3), including the intragranular pore dominant (IntraPD), micro fracture dominant (MFD), intergranular pore dominant (InterPD), and mixed pores systems (MP). The classification shows that the samples are dominated by InterPD and MP systems, followed by IntraPD one (Fig. 3).

The wide T_2 ranges (0.1–10000 ms) and varied T_2 distribution patterns including the unimodal, bimodal, and right-skewed bimodal patterns of the saturated samples (Fig. 4), indicate wide pore size ranges and differed pore constitutes in tight gas sandstone. The unimodal distribution pattern is characterized by a single peak in the range 0.1–100 ms, suggesting the dominant porosity contribution of small pores. This

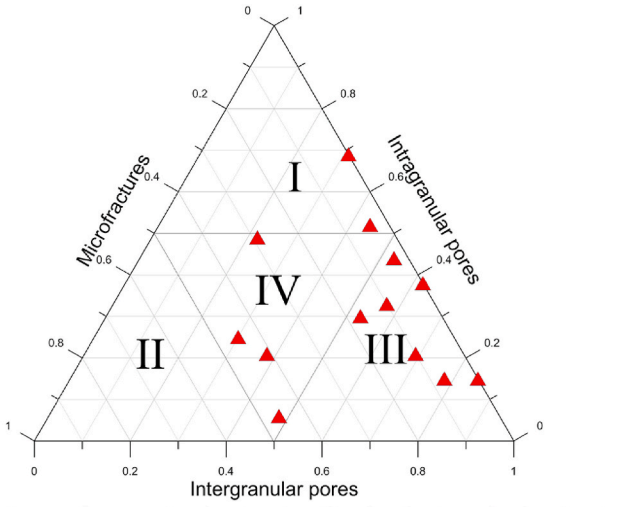

Fig. 3. Pore system types of the tight gas sandstone classified by the triangle charts.

Table 3
Constitutes of pore types in the tight sandstone samples.

Sample	P-interG (%)	D-interG (%)	D-intraG (%)	InterC (%)	MF (%)
1	38.0	10.0	1.0	5.0	46.0
4	41.0	28.0	16.0	5.0	10.0
5	2.0	51.0	31.0	13.0	3.0
6	70.0	15.0	8.0	7.0	0
8	3.0	28.0	39.0	30.0	0
11	1.0	21.0	11.0	38.0	29.0
12	49.0	29.0	8.0	7.0	7.0
15	3.0	35.0	10.0	11.0	41.0
20	13.0	21.0	12.0	13.0	45.0
23	26.0	36.0	29.0	9.0	0
25	11.0	33.0	16.0	36.0	4.0
26	26.0	31.0	8.0	25.0	10.0
27	4.0	49.0	5.0	25.0	17.0

Note that P-inteG, D-interG, D-intraG, InterC, MF refer to primary intergranular pore, dissolution intergranular pore, dissolution intragranular pore, intercrystalline pore, and micro fractures, separately.

pattern is common in the IntraPD samples with low porosity and ultralow permeability (Figs. 3 and 4, Table 1). A secondary peak emerges in the range 100–1000 ms in the bimodal distribution pattern, indicating the increasing porosity contributions of InterGs and MFs (Fig. 4 C). The peaks shift to the ranges of 1–1000 ms and amplitudes of the right peaks increase evidently in the right-skewed bimodal distribution patterns, suggesting the porosity is dominated by the InterGs and MFs (Fig. 4 D). The samples with bimodal distribution patterns are generally characterized by greater porosity and permeability and their pore systems are dominated by MP or InterPD systems (Table 1). With increasing permeability, the peaks of the T_2 distributions show an increasing trend and their patterns change from unimodal to right-skewed bimodal (Fig. 4 B–D). However, some exceptions occur, some samples with low permeability have relative great T_2 peaks and bimodal distributions. This is probably attributed to the presences of MFs.

Fig. 5 displays the three dimensional X-ray CT grayscale images and binary color-labelled images, showing the spatial distribution and location of pore spaces extracted from the rock matrix. The pore system of sample 11 with low porosity and ultralow permeability is dominated by irregular tiny pores and characterized by disperse spatial distribution (Fig. 5 E). Moreover, the large intergranular pores in it have irregular shapes with rough surface owing to the pore fillings (Figs. 4 B, Fig. 5 E). The pore constituents agree with the unimodal T_2 distribution pattern. The proportions of large pores rise evidently in the sample 6 and 12 and their pore systems exhibit regular pore shapes and connected spatial distributions (Fig. 5 F and G). There are a few amounts of tiny IntraGs in the system, which may serve as short channels bridging the InterGs. MFs show their appearances in the samples, having tabular shapes and may connect plenty of pores. They dramatically enhance the pore connectivity. However, the large pores and MFs become dominant in sample 1, resulting in right-skewed bimodal T_2 distribution pattern (Figs. 4 D, Fig. 5 H).

The volume fraction and quantity frequency distributions of the pore diameter in Fig. 6 suggest wide pore sizes ranging from 5.0 to 800 μm and varied contents of different-sized pores in tight gas sandstone. Similarity can be discovered when the volume fraction distributions are classified according to the T_2 distribution patterns. The Samples 5, 8, 11, and 25 with unimodal T_2 distribution are characterized by left-skewed volume fraction distribution patterns with pore sizes in the range 5–400 μm and average pore diameters between 10.85 and 13.69 μm (Fig. 6 A). The curves become fluctuated in samples with bimodal T_2 distributions (e.g. samples 4, 6, and 12). The evident proportional increases in the interval of 200–600 μm on the curves confirm the growing porosity contributions of InterGs and MFs (Fig. 6 B). Their average pore diameter increases to 12.74–14.51 μm. When it comes to the samples 1 and 20, the peaks move to the range 300–800 μm and average pore diameter rises to 15.66 μm, indicating the dominant roles of the InterGs

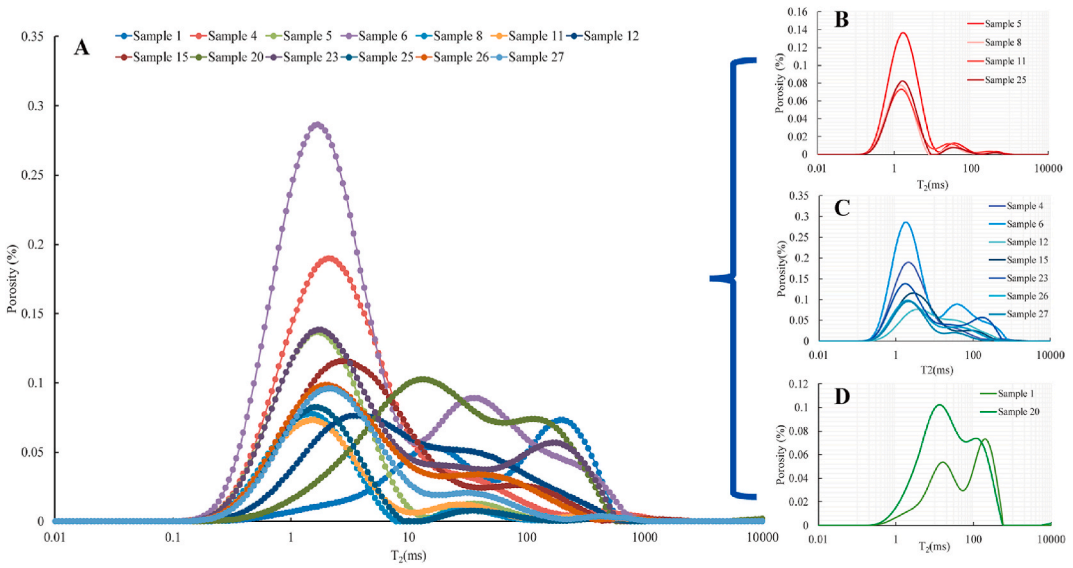

Fig. 4. (A) NMR T_2 distributions of saturated tight gas sandstone samples. (B) Unimodal T_2 distribution patterns, (C) bimodal T_2 distribution patterns, and (D) right-skewed bimodal T_2 distribution patterns.

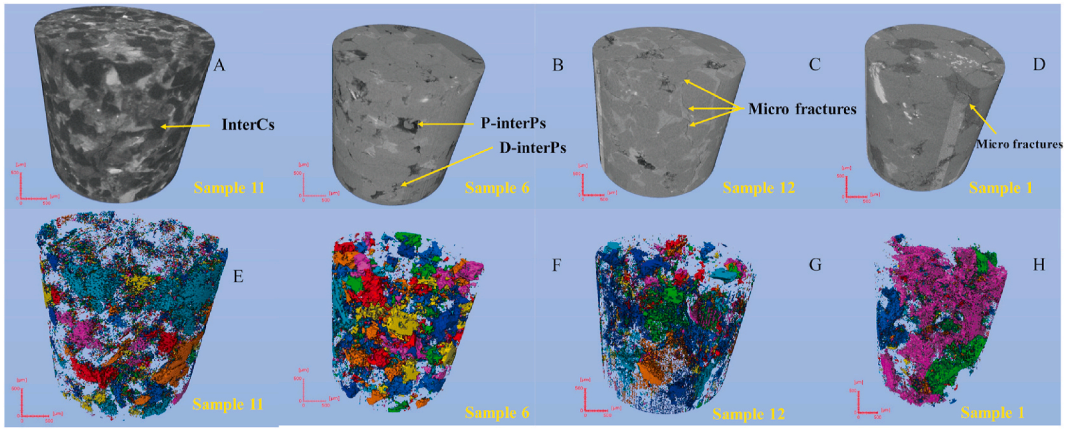

Fig. 5. Reconstructed grayscale images (A–D) and segmented binary color-labelled images (E–H) derived from the X-ray CT.

and MFs in their pore system (Fig. 6 C). However, the quantity frequency distributions of the samples are predominantly characterized by unimodal distribution patterns with peaks between 15 and 20 μm, suggesting high similarities in pore quantity of tight gas sandstone (Fig. 6 D).

3.3. Pore-scale heterogeneity

According to the fractal theory, the pores sharing similar fractal characteristic should follow a linear correlation on the double logarithmic plots of cumulative volume fraction of the pores (ϕ_c) against T_2 (illustrated by eight samples, e.g. sample 8, 4, 1, and etc.) (Fig. 7). The fractal curve is not a single line but can be broken into several segments at certain T_2 values (namely, fractal inflection points (FIP)), which agrees with the multi-fractal behaviors of low permeability sandstone. The results show that the tight sandstone is dominated by tri-fractal structure, followed by bi-fractal structure (Lai and Wang, 2015; Xia et al., 2019). The fractal dimensions for different-sized pores can be derived using the slopes of the linear segments, which can be divided into D_1, D_2, and D_3 from the shorter to longer T_2 domains (Fig. 7, Table 4). The D_1 ranges from 0.34 to 0.93 (avg. 0.58), much smaller than 2, implying the small-sized InterCs and IntraGs do not follow the fractal model described in Eq. (1). However, the values could be used to describe the heterogeneity of these small-sized pores (Amaefule et al., 1993; Gao and Li, 2016; Li, 2010). The D_2 is in the range 2.09–2.62 (avg. 2.39), suggesting the medium-sized D-interGs and MFs follow the fractal principle. The differential value between the maximum and minimum values (0.53) is smaller than that of D_1 (0.58), indicating that the pores are more self-similar with increasing size. The D_3 increases to the range 2.72–2.97 (avg. 2.90), suggesting the large-sized P-interGs and D-interGs are more self-similar. The bi-fractal structure presents in the unimodal and bimodal T_2 distributions but disappears in right-skewed bimodal T_2 distribution (Fig. 7). The fractal dimensions show decreasing trends from the unimodal to right-skewed bimodal T_2 distribution patterns with average D_1 decreasing from 0.70 to 0.47, average D_2 from 2.45 to 2.16, and average D_3 from 2.96 to 2.78. As the fractal dimension value is positively correlated with heterogeneity degree (Li, 2010; Wang et al., 2018), it can be inferred that the tight sandstone dominated by IntraPD system with unimodal T_2 distribution is characterized by strongest pore-scale heterogeneity. The samples dominated by InterPD and MFD systems with right-skewed bimodal T_2 distributions have more homogeneous structures (Fig. 7 G and H).

3.4. Fluid accessibility

The significant amplitude differences between the saturation and centrifugation T_2 spectrums in Fig. 8 exhibit the fluid accessibility of the

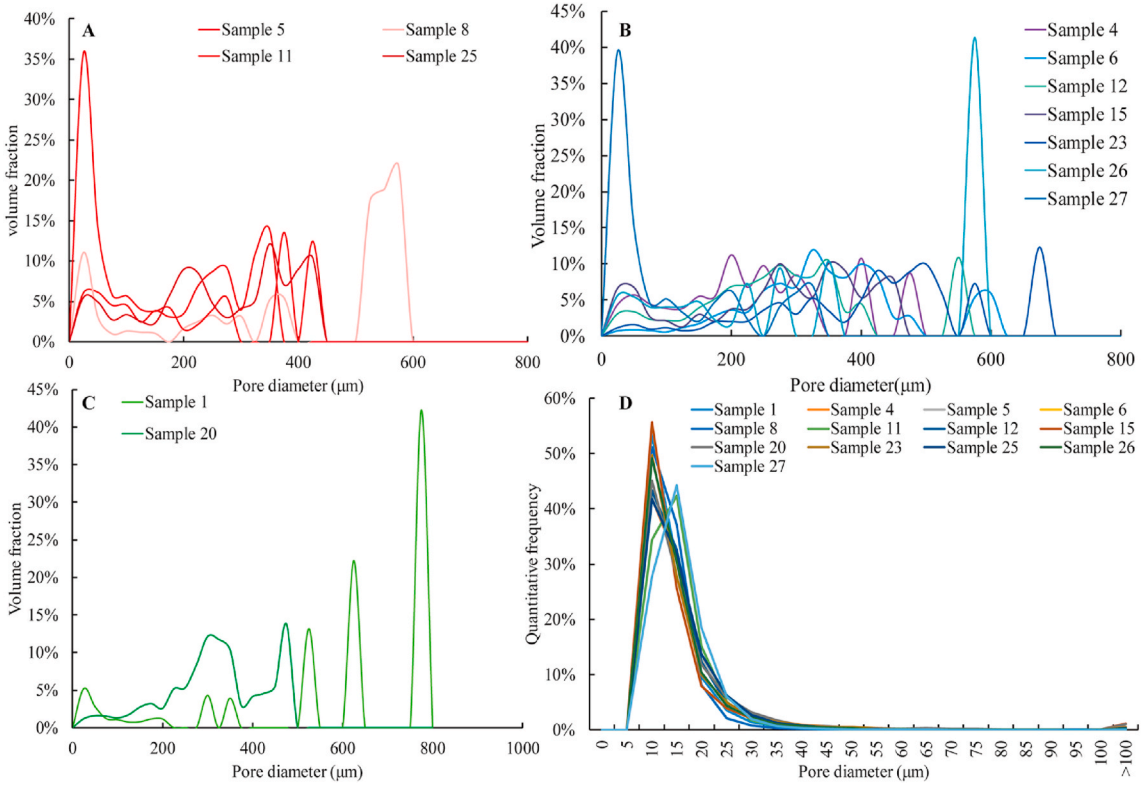

Fig. 6. Volume fraction distributions of pore size for the samples with unimodal T_2 patterns (A), bimodal T_2 patterns (B), right-skewed bimodal T_2 patterns (C). Quantitative frequency distributions of pore size of the tight gas sandstone samples (D).

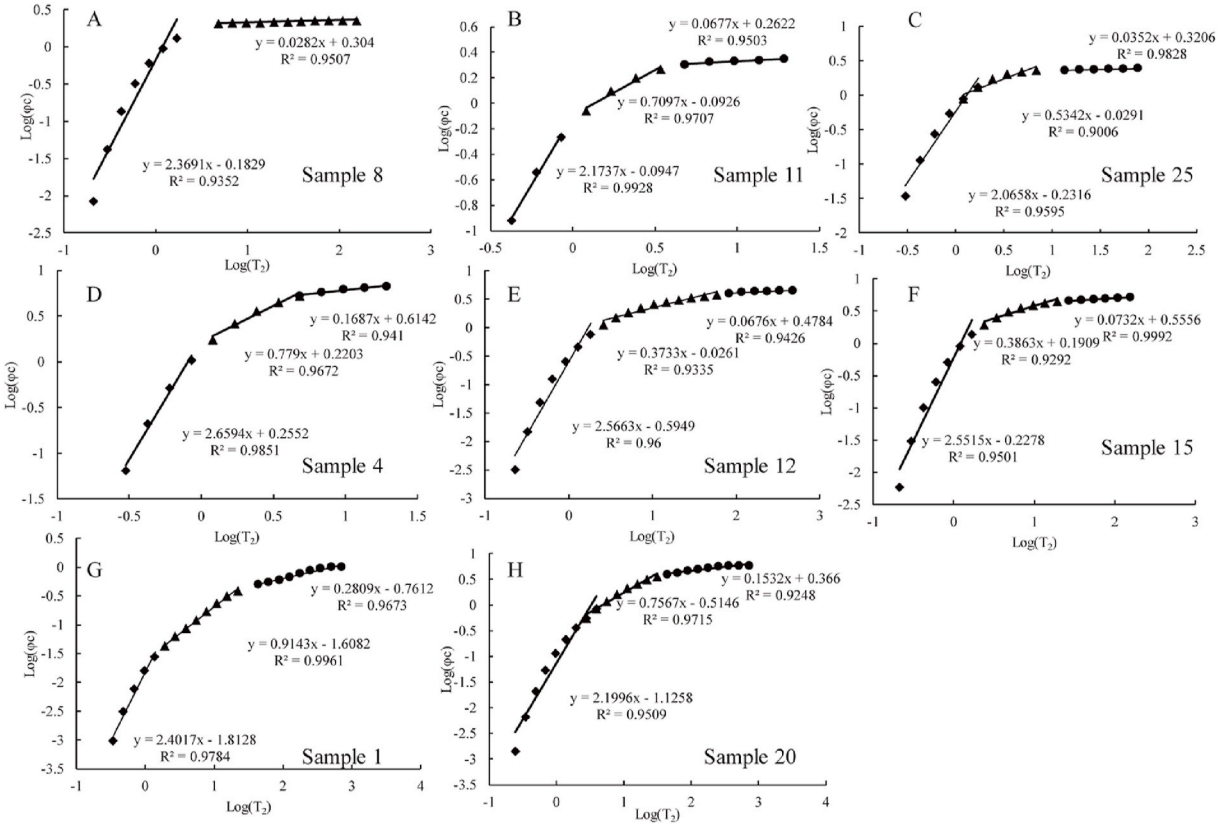

Fig. 7. Fractal curves of eight tight gas sandstone samples on the plots of Log (T_2) vs Log (ϕ_c).

Table 4
Pore fractal dimensions of the tight sandstone samples obtained from NMR.

Sample	D_1	D_2	D_3	D_{avg}
1	0.60	2.09	2.72	1.80
4	0.34	2.22	2.83	1.76
5	0.43	2.60	2.97	2.00
6	0.41	/	2.86	1.63
8	0.63	/	2.97	1.80
11	0.83	2.29	2.93	2.02
12	0.43	2.63	2.93	2.01
15	0.45	2.61	2.93	2.00
20	0.80	2.24	2.85	1.96
23	0.56	/	2.91	1.73
25	0.93	2.47	2.96	2.12
26	0.65	2.34	2.92	1.97
27	0.47	2.52	2.93	1.97

Note that D_1, D_2, D_3 are the fractal dimensions for small-sized pore, medium-sized pore, and large-sized pore, respectively. D_{avg} is the average value of D_1, D_2, and D_3.

pores of certain sizes. The accessible fluid saturation of the whole pore system of tight sandstone can be calculated using Eq. (2), which is between 8.39 and 43.87% (avg. 23.69%). The fluid accessibilities show evident differences among the samples. The samples 5, 8, 11, and 25 with unimodal T_2 distributions patterns are characterized by low fluid accessibilities with accessible saturations between 8.39 and 17.08% (avg. 12.2%). Samples 4, 6, 12 and etc. with bimodal T_2 distributions exhibit better fluid accessibilities with accessible saturation ranging from 16.33 to 40.24% (avg. 25.19%). The accessible saturations rise to the range of 39.28–43.87% (avg. 41.58%) in samples 1 and 20 with right-skewed bimodal T_2 distributions (Fig. 8).

$$S_f = \frac{\int_0^{T_{max}} f_1(T_2)d(T_2) - \int_0^{T_{max}} f_2(T_2)d(T_2)}{\int_0^{T_{max}} f_1(T_2)d(T_2)} \times 100\% \quad (2)$$

where the S_f is the fluid accessible saturation, %; $f_1(T_2)$ and $f_2(T_2)$ are the functions showing the amplitudes at certain T_2 value on the saturation T_2 spectrums and on the centrifugation T_2 spectrums, respectively.

The FIPs on the fractal curves provide an excellent way to evaluate the fluid accessibilities of pores in certain size ranges on the T_2 spectrums. Accordingly, the accessible saturations of small-sized, medium-sized, and large-sized pores can be separately expressed by Eqs. (3)–(5), and their accessibility contributions are obtained employing Eq. (6). Inaccessible proportions, ratios between covering areas of centrifugation spectrums to those of saturation spectrums in certain T_2 ranges of different-sized pores, are derived using Eqs. (7)–(9).

$$S_s = \frac{\int_0^{T_1} f_1(T_2)d(T_2) - \int_0^{T_1} f_2(T_2)d(T_2)}{\int_0^{T_1} f_1(T_2)d(T_2)} \times 100\% \quad (3)$$

$$S_m = \frac{\int_{T_1}^{T_2} f_1(T_2)d(T_2) - \int_{T_1}^{T_2} f_2(T_2)d(T_2)}{\int_{T_1}^{T_2} f_1(T_2)d(T_2)} \times 100\% \quad (4)$$

$$S_l = \frac{\int_{T_2}^{T_{max}} f_1(T_2)d(T_2) - \int_{T_2}^{T_{max}} f_2(T_2)d(T_2)}{\int_{T_2}^{T_{max}} f_1(T_2)d(T_2)} \times 100\% \quad (5)$$

whereS_s, S_m, and S_l separately represent the fluid accessible saturations of small-sized, medium-sized, and large-sized pores; T_1 and T_2 are the transverse relaxation times corresponding to the FIP_1 and FIP_2 between small-sized and medium-sized pores, and medium-sized and large-sized pores, respectively.

$$C = \frac{S_p}{S_f} \times 100\% \quad (6)$$

where C is the accessibility contribution of certain-sized pores, S_p is the fluid accessible saturation of certain-sized pores.

$$R_{is} = \frac{\int_0^{T_1} f_2(T_2)d(T_2)}{\int_0^{T_1} f_1(T_2)d(T_2)} \times 100\% \quad (7)$$

$$R_{im} = \frac{\int_{T_1}^{T_2} f_2(T_2)d(T_2)}{\int_{T_1}^{T_2} f_1(T_2)d(T_2)} \times 100\% \quad (8)$$

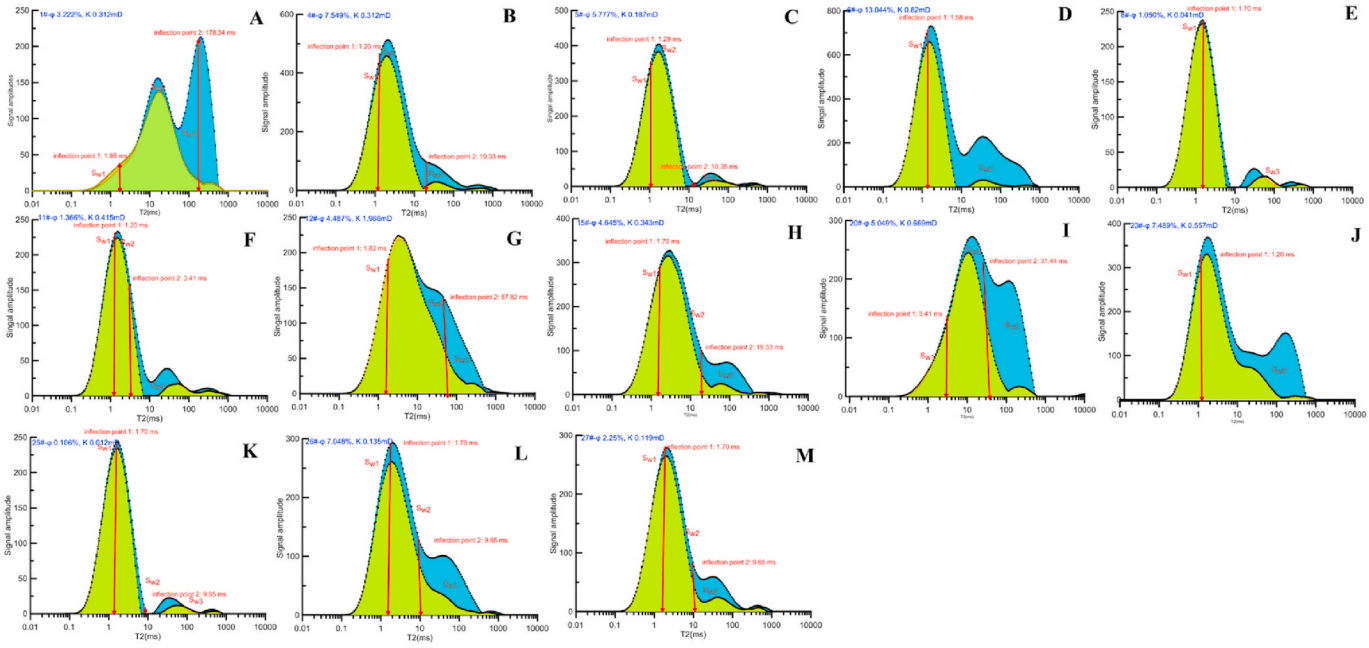

Fig. 8. Fluid accessibilities of tight gas sandstone samples evaluated by the saturated and centrifuged T_2 spectrums (Note that the yellow and blue areas represent the inaccessible proportion and accessible proportion of pores, respectively. The red lines mark the fractal inflection points. S_{W1}, S_{W2}, and S_{W3} separately represent the accessible proportions of the small-sized, medium-sized, and large-sized pores).

$$R_{il} = \frac{\int_{T_2}^{T_{max}} f_2(T_2)d(T_2)}{\int_{T_2}^{T_{max}} f_1(T_2)d(T_2)} \times 100\% \quad (9)$$

where R_{is}, R_{im}, and R_{il} are the inaccessible proportions for the small-sized, medium-sized, and large-sized pores, separately.

The fluid accessibility parameters suggest best fluid accessibility of large-sized pores in tight sandstone, with accessible saturation in the range 3.19–38.86% (avg. 16.40%), accessibility contributions ranging from 29.59 to 96.56% (65.73%), and inaccessible proportions between 8.00 and 83.00%. The medium-sized pores have moderate fluid accessibilities, which have accessible saturations in the range 4.93–23.83%, accessibility contributions of 14.46–58.96%, and inaccessible proportions of 67.00–94.00%. However, the small-sized pores are characterized by poor fluid accessibility with most of them are disconnected (inaccessible proportions between 0.92 and 1.26). The accessible saturations and accessibility contributions are below 2.5% and 15%, respectively. Notably, abnormality occurs in some samples, of which the small-sized pores have inaccessible proportions >1 and negative accessible saturations. The transportation of movable water from relative large pores to the tiny pores under the centrifugation pressure is probably responsible for this phenomenon, which is likely determined by the strong hydrophilia of clay minerals and connectivity of InterCs. The accessible saturations and accessibility contributions of medium- and large-sized pores show descending trends from the right-skewed bimodal to unimodal T_2 distribution patterns, while their inaccessible ratios exhibit opposite trends. Negative accessible saturation values of small-sized pores generally present in right-skewed bimodal T_2 distribution samples owing to their relative good pore connectivity. The results indicate that the fluid accessibilities of tight gas sandstone are dominated by large-sized pores, followed by medium-sized pores. Differences in the fluid accessibilities of large- and medium-sized pores are responsible for the fluid accessibility distinctions of different tight sandstone samples (Fig. 8).

4. Discussion

4.1. Origins and controls of pore-scale heterogeneity

The fractal structures of tight sandstone are various. The fractal dimension variations of certain-sized pores and pore systems among the samples suggest the significant differences in the pore-scale heterogeneity, which probably originate from the components, textures, and pore microstructures variations.

4.1.1. Impacts originated from mineralogy

The correlations between the fractal dimensions and mineral contents suggest that small-sized pores become more heterogeneous with the decrease of rigid grains (Fig. 9 A), and increase of ductile grains (Fig. 9 D) and carbonate cements (Fig. 9 I). However, the heterogeneity decreases with the clay contents because the InterCs generally exhibit pretty regular structures, orientations, and appearances in the dominant clay minerals of kaolinite and chlorite observed in the investigated tight sandstone (Fig. 9 G and H).

The correlations become complicated in medium-sized pores. The heterogeneity of medium-sized pores is negatively correlated with content of quartz and feldspar when it is less than 65%, but shows two opposite correlations when it is greater than 65%. The positive correlation is probably attributed to the increase of the MFs induced by increasing brittleness (Fig. 9 A). This phenomenon can be supported by the observations of a few amount of MFs (Fig. 9 B) and massive MFs (Fig. 9 C) in the samples with high rigid grain contents. The medium-sized pores heterogeneity rises with increase of clay and carbonate contents as the pore-filling clay aggregates and carbonate cementation will complicate the geometry and morphology, and roughen the smoothness of the surface of IntraGs and MFs (Fig. 9 G and I). However, the poor correlation between D_2 and rock fragments suggests that the ductile particles have negligible influences on the heterogeneity of medium-sized pores (Fig. 9 D).

A poor correlation is discovered between D_3 and the content of rigid grains (Fig. 9 A), which is attributed to the influence of irregular D-

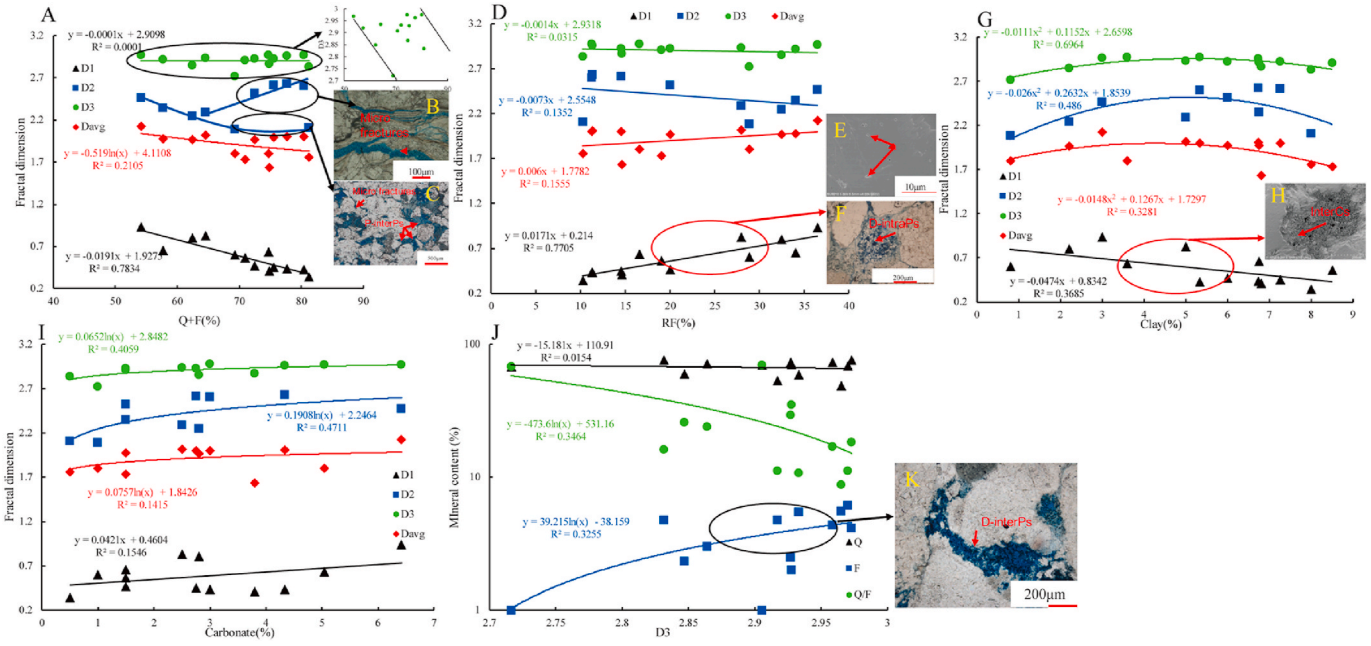

Fig. 9. Effects of mineralogy on the pore-scale heterogeneity. (A) Correlations between content of rigid grain (quartz and feldspar) and D_1, D_2, D_3, and D_{avg}. (B) Large quantity of micro fractures induced by natural fracturing. (C) A few amount of micro fractures with low heterogeneity. (D) Correlations between ductile rock fragment and D_1, D_2, D_3, and D_{avg}. (E) and (F) dissolution intragranular pores. (G) Correlations between clay and D_1, D_2, D_3, and D_{avg}. (H) Homogeneous intercrystalline pores between dominant kaolinite. (I) Correlations between carbonate and D_1, D_2, D_3, and D_{avg}. (J) Correlations between D_3 and quartz, feldspar, and quartz/feldspar. (K) Dissolution intergranular pores with irregular pore outlines and rough surfaces.

interGs generated from feldspar dissolution (Fig. 9 B, K). The positive correlation between D_3 and feldspar and negative correlation between it and quartz/feldspar imply that the P-interGs preserved are favorable for the homogeneity of the large-sized pores, while D-interGs are on the contrary (Fig. 9 B, J, K). The effects of clay on the heterogeneity of large-sized pores reverse with increasing content. The rising clay content roughens the surface and complicates the pore shapes in low content of less than 5%, but may enhance the self-similarity with the increasing filling degree (Fig. 9 G). The positive phenomenon will be enhanced if the clay minerals is dominated by chlorite owing to its benefits for the preservation of the P-interGs. Greater carbonate content always unfavorable for the homogeneity of the large-sized pores (Fig. 9 I). The mineralogy variation is one of the controls for the complex pore-scale heterogeneity as the same kind of minerals may exert completely different impacts on different-sized pores (Fig. 9).

The correlations between the D_{avg} (average of D_1, D_2, and D_3) and mineral contents suggest that the system heterogeneity is negatively correlated with the quartz content (Fig. 9 A), but positively correlated with contents of feldspar, rock fragment, and carbonate (Fig. 9 D, G, I, J). Similar trends are found between D_{avg} and clay, and D_3 and clay (Fig. 9 G). The effects of mineralogy on the system heterogeneity are similar to those on large-sized pores, indicating the heterogeneity of the whole pore network of tight sandstone is dominated by the large-sized pores.

4.1.2. *Effects originated from petrology*

The arrangements and textures of the matrix grains also influence the geometry and morphology of the pores (Ajdukiewicz and Lander, 2010; McKinley et al., 2011; Mozley et al., 2016), which will exert impacts on the pore-scale heterogeneity. The negative correlation between D_1 and median grain size suggests that greater grain size is favorable for the homogeneity of the small-sized pores. However, the poor positive correlation between D_1 and sorting coefficient indicates that worse sorting will result in heterogeneity increases (Fig. 10 A, B). The poor negative correlation between D_1 and skewness confirms the benefits of greater grain sizes on the homogeneity of small-sized pores. The reversal of all of the correlations in medium-sized pores suggests that greater grain size and better sorting increase the heterogeneity of medium-sized pores (Fig. 10 A–C). Similar effects occur in large-sized pores (Fig. 10 A–C). The grain size exerts a poor influence on the system heterogeneity compared with sorting coefficient (Fig. 10). The D_{avg} rises with the sorting coefficient before 2.3 and then decreases evidently, which may be attributed to the opposite effects of sorting on the heterogeneities of small-sized and medium- to large-sized pores (Fig. 10 B).

4.1.3. *Origins from pore attributes*

As the fractal dimension is a direct description of pores, the pore attributes definitely exert direct effects on the pore-scale heterogeneity. The effects of pore types are evaluated by investigating the relationships between the fractal dimensions of certain-sized pores and contents of their dominant pore types. The negative correlation between content of P-interGs and D_3 indicates the primary pores can reduce the heterogeneity of the large-sized pores (Fig. 11 A). The D-interGs exert opposite effects as they complicate the shapes and edges, and roughen the smoothness of the surfaces (Fig. 11 B). Negative effects of D-intraGs on the heterogeneity of medium-sized pores are discovered owing to the pore complexity enhancements originated from dissolution (Fig. 11 C). However, the presence of MFs benefits the homogeneity of medium-sized pores (Fig. 11 D). The heterogeneity of small-sized pores rises with the increasing contents of InterCs and D-intraGs (Fig. 11 E). The relationships between the D_{avg} and contents of pore types suggest the system heterogeneity is strongly influenced by the P-interGs, MFs, and InterCs, but barely not affected by the D-intraGs (Fig. 11).

The pore geometries are analyzed based on the pore size classification proposed, which divides the pores into small-micropores with diameters <20 μm, mesopores with diameter between 20 and 40 μm, and macropores with diameter >40 μm (Qiao et al., 2017). The volume fractions, quantity frequencies, and average pore radii of the three types of pores are separately calculated employing the PNM data (Table 5). The impacts of the geometries of small-micro pores, mesopores, and macropores on the D_1, D_2, and D_3 are separately evaluated in Fig. 12. The results reveal that the heterogeneity of small-sized pores is determined by the diameters of the small-micro pores (positive correlation) (Fig. 12 B), followed by its volume fraction (Fig. 12 A), but is barely not affected by its quantity (Fig. 12 C). Heterogeneity of medium-sized pores is dominated the quantity of the mesopore (positive correlation) (Fig. 12 D–F). Heterogeneity of large-sized pores is dominated by the quantity of macropores and is negatively correlated with their volume fractions and pore diameters (Fig. 12 G–I). The D_{avg} increases with the volume fraction of small-micropores and mesopores and diameter of small-micropores, but decreases with the volume fraction, diameter, and quantity of the macropores (Fig. 12), suggesting opposite effects of the pore geometries of the large-sized pores and medium- to small-sized pores on the system heterogeneity.

The ratio of pore volume to surface area (V/S) and aspect ratio (AR) of the three types of pores (Table 6) are separately plotted with the D_1, D_2, D_3, and D_{avg} in Fig. 13. Because of the different morphology variations of the D-intraGs and InterCs, the heterogeneity of small-sized pores exhibits different correlation trends with the increasing of V/S of small-micro pores (Fig. 13 A). The heterogeneity of medium-sized pores is poorly correlated with the morphologies of the mesopores, which may be attributed to the different morphology characteristics of D-intraGs and MFs (Fig. 13 B and E). D_3 shows better relationships with morphologies of macropores. Its negative correlation with V/S and positive correlation with AR suggest that roundness and smoothness improvements bring reductions to heterogeneity of the large-sized pores (Fig. 13 C and F). The system heterogeneity is mainly affected by morphologies of small-micro pores and macropores, but barely not influenced by that of the mesopores (Fig. 13).

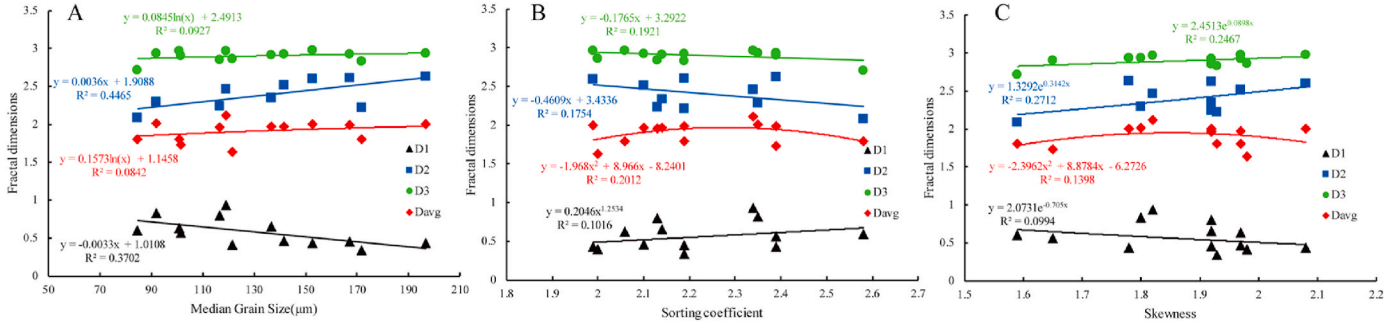

Fig. 10. Effects of grain textures on the pore-scale heterogeneity. Correlations between median grain size (A), sorting coefficient (B), skewness (C) and fractal dimensions.

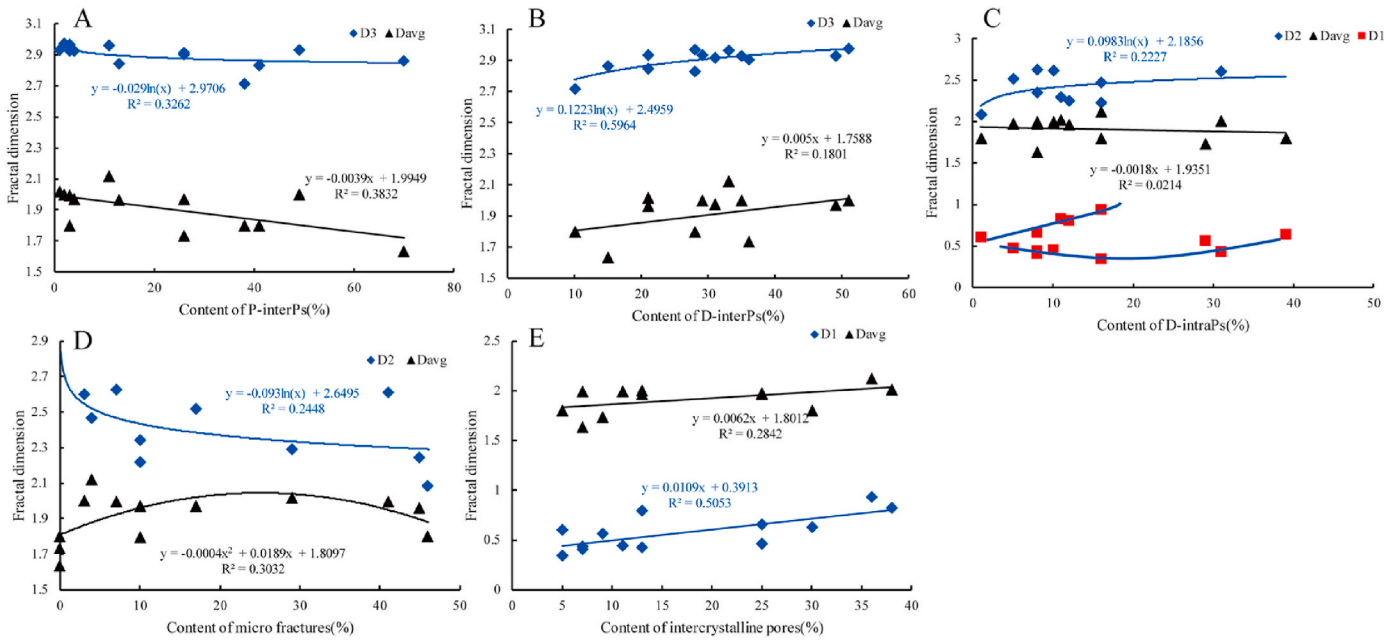

Fig. 11. Effects of pore genetic types on the pore-scale heterogeneity. Impacts of contents of primary intergranular pores (A) and dissolution intergranular pores (B) on the heterogeneities of large-sized pores and pore system. Influences of content of dissolution intragranular pores (C) on the heterogeneities of medium-sized pores, small-sized pores, and pore system. (D) Effects of content of micro fractures on the heterogeneities of medium-sized pores and pore system. (E) Correlations between content of intercrystalline pores and heterogeneities of small-sized pores and pore system.

Table 5
Pore geometrical parameters derived from X-μCT.

Sample	VF_s	VF_{me}	VF_{ma}	D_s(μm)	D_{me}(μm)	D_{ma}(μm)	Q_s	Q_{me}	Q_{ma}
1	0.04	0.03	0.93	10.10	25.10	93.79	0.93	0.03	0.04
4	0.03	0.05	0.92	10.83	26.23	76.11	0.86	0.12	0.03
5	0.04	0.06	0.90	10.80	25.71	72.91	0.87	0.11	0.02
6	0.01	0.01	0.99	9.89	26.48	124.10	0.89	0.08	0.03
8	0.09	0.04	0.87	10.20	24.78	87.25	0.96	0.03	0.00
11	0.27	0.20	0.53	11.39	24.53	63.19	0.92	0.08	0.00
12	0.02	0.03	0.95	10.75	26.26	86.58	0.88	0.09	0.02
15	0.04	0.07	0.89	11.45	25.68	72.89	0.84	0.14	0.02
20	0.01	0.01	0.98	10.56	26.18	102.04	0.85	0.12	0.04
23	0.01	0.01	0.98	10.29	26.45	93.98	0.88	0.10	0.03
25	0.04	0.05	0.91	10.91	25.53	79.46	0.87	0.11	0.02
26	0.04	0.05	0.91	10.40	26.10	72.54	0.90	0.08	0.02
27	0.30	0.22	0.48	11.93	24.46	63.74	0.91	0.09	0.00

Note that VF_s, VF_{me}, and VF_{ma} are the volume fractions for small-micro pore, mesopore and macropore, separately. D_s, D_{me}, and D_{ma} are the diameters of small-micro pore, mesopore and macropore, separately. Q_s, Q_{me}, and Q_{ma} are the quantity frequencies of small-micro pore, mesopore and macropore, separately.

4.2. Impacts of pore-scale heterogeneity

4.2.1. Effects of pore-scale heterogeneity on the fluid accessibility

The significant differences in the fluid accessibilities of the investigated tight sandstone samples can be attributed to the complex interplays between pore structure and fluid flow. However, the physics governing the fluid accessibility in tight porous media have been poorly understood owing to the influences of extreme pore-scale heterogeneity.

The correlation analyses between the fractal dimensions and fluid accessibility parameters of certain-sized pores in Fig. 14 indicate that the heterogeneity of the small-sized pores barely not affects their own fluid accessibility. The poor influence is probably attributed to the extra strong impacts of the clay hydrophilia as the clay minerals are the dominant host for these pores. However, the heterogeneities of medium- and large-sized pores strongly influence their own fluid accessibilities (Fig. 14 B and C). The inaccessible proportions of medium to large-sized pores have positive correlations with their fractal dimensions, while the accessible saturations exhibit descending trend with increasing dimension values. This suggests the increase of heterogeneity is unfavorable for the fluid accessibilities of these pores. The correlations between the accessibility contributions of different-sized pores and their own fractal dimensions suggest that a moderate heterogeneity of large-sized pores may enhance the fluid flow inside the large InterGs. However, the heterogeneity of medium-sized pores exert complex influences on their fluid accessibility contributions. Their heterogeneity increases at a low value range (<2.35) may reduce the fluid flow inside them, but the heterogeneity increases at a high value range (>2.35) brings fluid flow enhancement due to the presence of the MFs (Fig. 14 B).

The rising correlation coefficients between the fractal dimensions and their fluid accessibilities from small- to large-sized pores suggest the effects of pore-scale heterogeneity on the pore-scale fluid mobility increase with the pore size (Fig. 14A–C). The correlations between total accessible saturation and D_1, D_2, D_3, and D_{avg} indicate that the system fluid accessibility is dominated by the heterogeneity of the large-sized pores, followed by the medium-sized pores, but is barely not affected by the small-sized pores (Fig. 14 D).

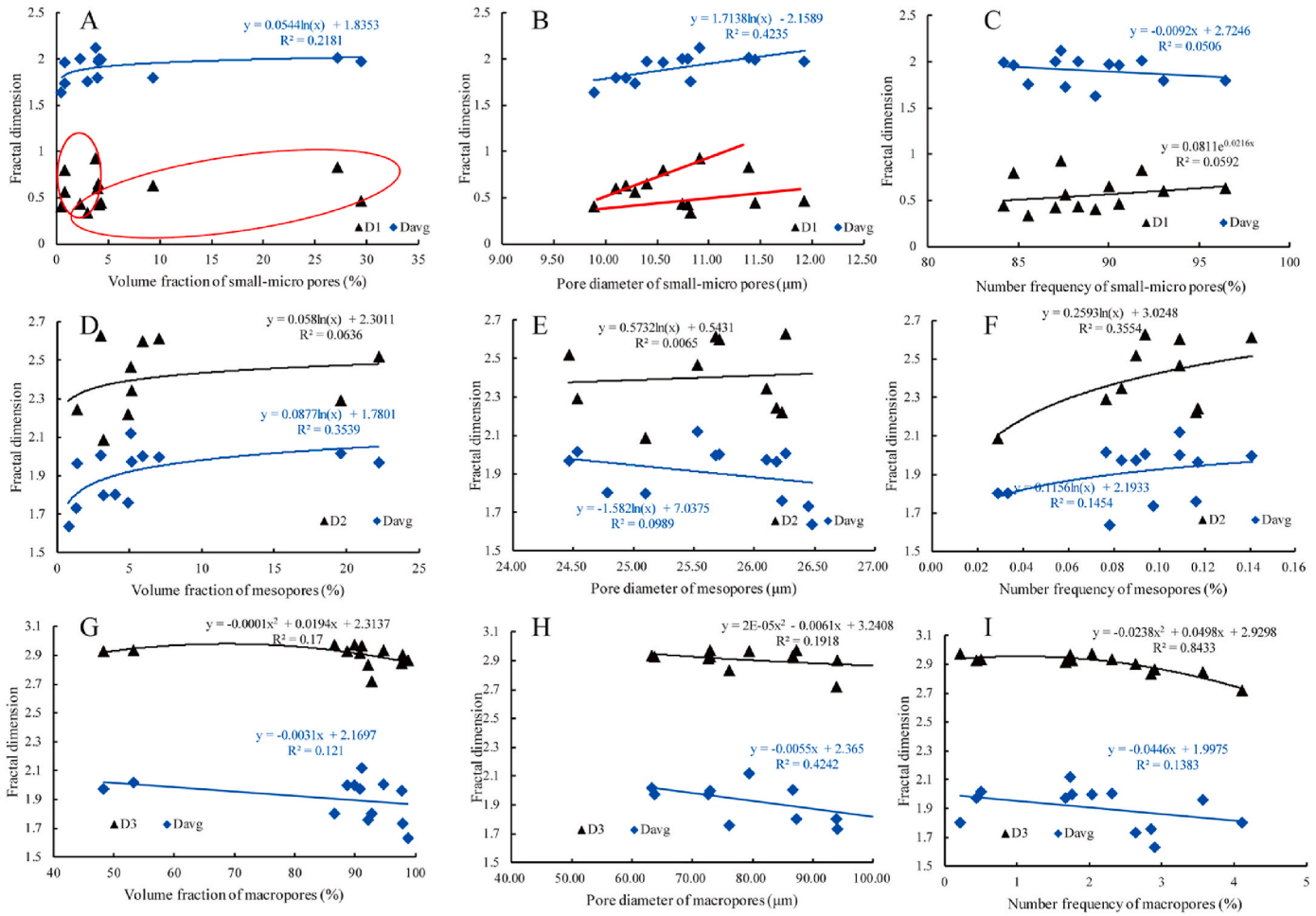

Fig. 12. Effects of pore geometry on the pore-scale heterogeneity. The correlations between volume fraction (A), pore diameter (B), and number frequency (C) of small-micropores and D_1 and D_{avg}. The correlations between volume fraction (D), pore diameter (E), and number frequency (F) of mesopores and D_2 and D_{avg}. The correlations between volume fraction (G), pore diameter (H), and number frequency (I) of macropores and D_3 and D_{avg}.

Table 6
Pore morphological parameters derived from X-μCT.

Sample	V/S_s	V/S_{me}	V/S_{ma}	AR_s	AR_{me}	AR_{ma}
1	1.8	2.74	7.01	2.32	2.79	2.13
4	1.88	3.25	5.62	2.24	2.87	2.59
5	1.89	3.17	4.86	2.13	2.62	2.66
6	1.77	3.47	8.81	2.2	2.4	2.19
8	1.81	2.54	3.8	2.45	2.45	2.98
11	1.85	2.48	2.82	2.57	2.89	2.91
12	1.86	3.16	6.29	2.3	2.79	2.78
15	1.88	3.25	4.86	2.01	2.46	2.77
20	1.87	3.37	7.35	2.08	2.48	2.48
23	1.82	3.45	6.44	2.18	2.37	2.35
25	1.91	3.18	4.97	2.12	2.49	2.53
26	1.83	3.13	4.62	2.25	2.78	2.67
27	1.86	2.45	2.89	2.69	2.8	2.82

Note that V/S_s, V/S_{me}, and V/S_{ma} are the ratios of pore volume to pore surface area for the small-micro pores, mesopores and macropores, separately. AR_s, AR_{me}, and AR_{ma} are the aspect ratios of the small-micro pores, mesopores and macropores, separately.

4.2.2. New insights into the permeability estimation

Permeability serves as a direct macroscopic description of the fluid flow capacity of porous media. It has been regarded as a long-term focus in the evaluation of clastic hydrocarbon reservoirs. The fluid accessibility obtained from NMR allows a reliable way for the permeability estimation. The Coates model employing the relationship between porosity, free fluid index (FFI), and bound water volume index (BVI) obtained from NMR measurement is proposed and widely accepted (Eq. (10) and (11)). However, the performance of Coates model is not stable in the tight sandstone owing to its intricate pore structures. Based on the fluid accessibility evaluation applying the film bound water model and FIPs, the FFI and BVI can be separately divided into three parts and can be described by the following equations (Eq. (12) and (13)).

$$K = \left[\left(\frac{\phi}{C}\right)^2 \frac{FFI}{BVI}\right]^2 \tag{10}$$

$$LogK = A + BLog\phi + CLog\frac{FFI}{BVI} \tag{11}$$

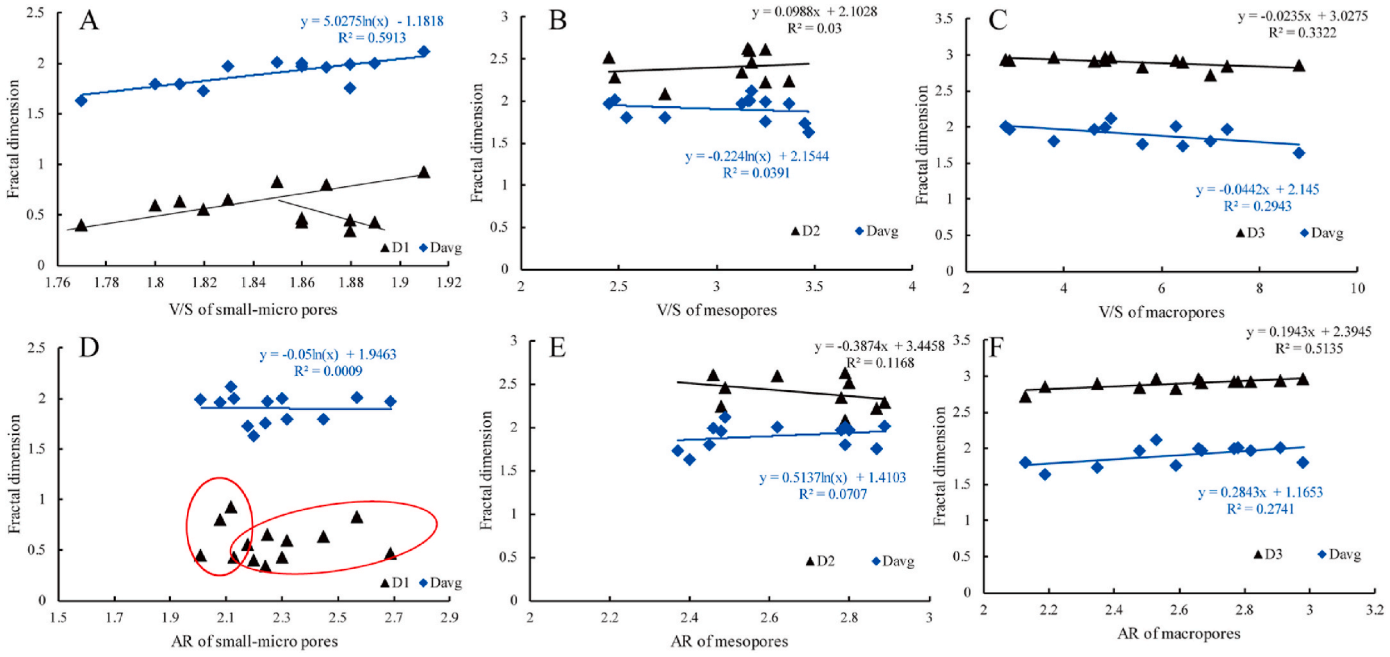

Fig. 13. Impacts of pore morphology on the pore-scale heterogeneity. Relationships between ratio of volume to surface area (V/S) (A) and aspect ratio (AR) (D) of small-micropores and D_1 and D_{avg}. Relationships between V/S (B) and AR (E) of mesopores and D_2 and D_{avg}. Relationships between V/S (C) and AR (F) of macropores and D_3 and D_{avg}.

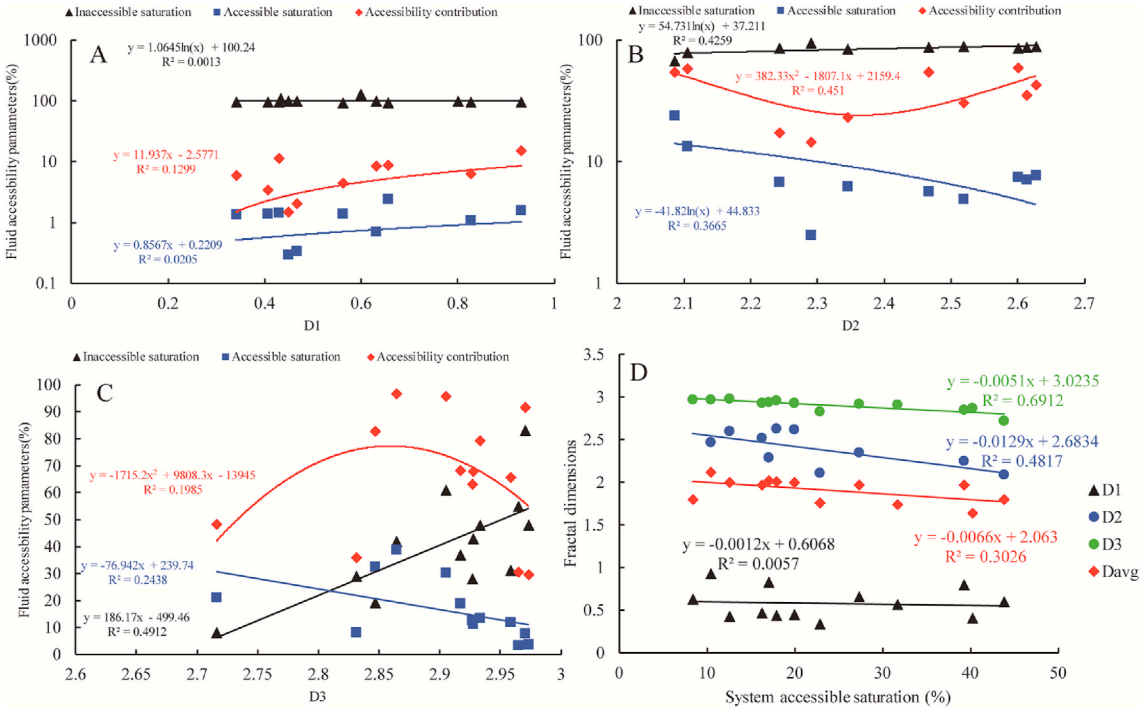

Fig. 14. (A) Correlations between inaccessible saturation, accessible saturation, and accessibility contribution of small-sized pores and D_1. (B) Correlations between inaccessible saturation, accessible saturation, and accessibility contribution of medium-sized pores and D_2. (C) Correlations between inaccessible saturation, accessible saturation, and accessibility contribution of large-sized pores and D_3. (D) Correlations between D_1, D_2, D_3, and D_{avg}, and system fluid accessibility.

$$FFI = S_W = \frac{\int_0^{T_{max}} f_1(T_2)d(T_2) - \int_0^{T_{max}} f_2(T_2)d(T_2)}{\int_0^{T_{max}} f_1(T_2)d(T_2)} = \frac{\int_0^{T_1} f_1(T_2)d(T_2) - \int_0^{T_1} f_2(T_2)d(T_2) + \int_{T_1}^{T_2} f_1(T_2)d(T_2) - \int_{T_1}^{T_2} f_2(T_2)d(T_2) + \int_{T_2}^{T_{max}} f_1(T_2)d(T_2) - \int_{T_2}^{T_{max}} f_2(T_2)d(T_2)}{\int_0^{T_{max}} f_1(T_2)d(T_2)} \quad (12)$$

$$BVI = S_i = \frac{\int_0^{T_{max}} f_2(T_2)d(T_2)}{\int_0^{T_{max}} f_1(T_2)d(T_2)} = \frac{\int_0^{T_1} f_2(T_2)d(T_2) + \int_{T_1}^{T_2} f_2(T_2)d(T_2) + \int_{T_2}^{T_{max}} f_2(T_2)d(T_2)}{\int_0^{T_{max}} f_1(T_2)d(T_2)} \quad (13)$$

According to the film bound water model, the $\int_0^{T_1} f_1(T_2)d(T_2) - \int_0^{T_1} f_2(T_2)d(T_2)$ is the covering area between the saturation and centrifugation T_2 spectrums when the T_2 is less than the transverse time of FIP_1 and can be simplified as A_{F0}. The $\int_{T_1}^{T_2} f_1(T_2)d(T_2) - \int_{T_1}^{T_2} f_2(T_2)d(T_2)$is the covering area between the saturation and centrifugation T_2 spectrums when the T_2 is between the transverse time of FIP_1 and that of FIP_2, which can be simplified as A_{F1}. $\int_{T_2}^{T_{max}} f_1(T_2)d(T_2) - \int_{T_2}^{T_{max}} f_2(T_2)d(T_2)$is the covering area between the saturation and centrifugation T_2 spectrums when the T_2 is greater than the transverse time of FIP_2, which can be simplified as A_{F2}. The $\int_0^{T_1} f_2(T_2)d(T_2) + \int_{T_1}^{T_2} f_2(T_2)d(T_2) + \int_{T_2}^{T_{max}} f_2(T_2)d(T_2)$ is the total covering area of the centrifugation spectrum and can be simplified as A_2. Therefore, the FFI/BVI can be expressed by Eq. (14).

$$\frac{FFI}{BVI} = \frac{A_{F0} + A_{F1} + A_{F2}}{A_2} \quad (14)$$

As the signal amplitude differences of small-sized pores are minor and even could be negative owing to the water transportation from large-sized to small-sized pores under the effects of centrifugal forces and strong hydrophillia of clay minerals, the $\int_0^{T_1} f_1(T_2)d(T_2) - \int_0^{T_1} f_2(T_2)d(T_2)$ in the FFI/BVI would result in misestimate of the fluid mobility. The A_{F0} should be neglected as it will lead to deviations in permeability estimation. Therefore, Eq. (14) can be transformed to Eq. (15).

$$\frac{FFI}{BVI} = \frac{A_{F1} + A_{F2}}{A_2} \quad (15)$$

Accordingly, the Coates model can be modified according to the amplitude differences between the saturation and centrifugation T_2 spectrums, which provide a more direct way for the permeability estimation from the NMR measurements.

$$LogK = A + BLog\phi + CLog\frac{A_{F1} + A_{F2}}{A_2} \quad (16)$$

When taking the effects of pore-scale heterogeneity on the fluid accessibility into consideration, the estimation can be expressed as following by taking the system fractal dimension into the account of fluid accessibility index.

$$LogK = A + BLog\phi + CLog\frac{A_{F1} + A_{F2}}{A_2} + DLogD_f \quad (17)$$

Multiple linear regression analysis is performed to determine the empirical relationships in Eq. (11) and Eq. (17) and to examine the performance of the improved Coates model. The empirical equations derived using the Coates model and modified Coates model are displayed in Table 7. The result shows that the empirical correlation for modified one gets higher regression coefficient than the original one, indicating that the consideration of the fluid accessibility of different-sized pores and effects of pore-scale heterogeneity improve the applicability of the Coates model. If the two outliers in the porosity and permeability correlation, i.e. sample 11 and 12 with extreme low

Table 7
Empirical correlations derived from the original and modified Coates models.

Model types	Empirical equations	R^2	Note
Original Coates	LogK = −0.8191 + 0.7970Logϕ+0.3260Log(FFI/BVI)	0.69	All of the samples
Original Coates	LogK = −0.7080 + 0.6773Logϕ+0.6122Log(FFI/BVI)	0.88	Excluding outliers
Modified Coates	LogK = −1.4806 + 0.8175Logϕ+0.4870Log(FFI/BVI)*+2.6886LogD_f	0.71	All of the samples
Modified Coates	LogK = −0.4229 + 0.6446 Logϕ+0.5757Log(FFI/BVI)*-0.9971LogD_f	0.90	Excluding outliers

Note that (FFI/BVI)* is the ratio between free fluid index and bound water volume index recalculated on the basis of fluid accessibility calibration.

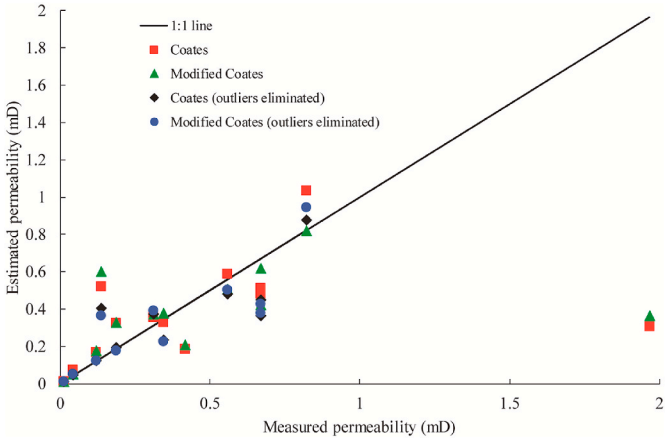

Fig. 15. Plots showing the deviations of the estimated permeability from the measured permeability.

porosity and high permeability, are eliminated from the regression, the coefficients of the original and modified Coates model rise evidently. Especially, the improved one shows an excellent performance with a coefficient of 0.90.

Fig. 15 plots the relationships between measured permeability and permeability estimated by the four empirical equations, where the deviations of the data points from the perfect 1:1 trend line indicate the performances of the estimations. We can figure out that the values estimated from improved Coates equations excluding the outliers show smaller deviations than the others, providing a more accurate permeability predication. This estimation enhancement from outlier exclusion suggests that the controlling factors of permeability in tight gas sandstone may be completely different and it is necessary to investigate the permeability variation mechanisms from the pore-scale perspective.

5. Conclusions

A logically combined analysis is conducted on the thirteen representative tight gas sandstone samples collected from the Permian Shanxi Formation of the Ordos Basin. The pore-scale heterogeneity of tight sandstone is investigated by NMR incorporating fractal theory. Its origins and controls are explored by combining mineralogy, petrology, and structural investigations through X-ray CT, CTS, SEM, and grain size analyses. Its impacts on the fluid flow are further evaluated by fluid accessibility evaluation. The conclusions can be drawn as follows.

The tight gas sandstone is characterized by intense pore-scale heterogeneity with multi-fractal structures dominated by tri-fractal, followed by bi-fractal, and wide ranges of fractal dimensions for small-sized , medium sized , large-sized pores , and pore system. The tight sandstones with intragranular pore dominant system and unimodal NMR T_2 distributions exhibit strongest pore-scale heterogeneity, while those of intergranular pore dominant and mixed pore systems with bimodal T_2 distributions have more homogeneous structures.

Pore-scale heterogeneity originates from pore attributes. The heterogeneity of large-sized pores is dominated by the macropore quantity, followed by it morphology and intergranular pore content. That of medium-sized pores is dominated by the mesopore quantity and strongly affected by the contents of dissolution intragranular pores and micro fractures. The heterogeneity of small-sized pores is determined by the intercrystalline pore content and size of small-micropore. The system heterogeneity is a coupled expression of the genesis, geometry, and morphology of different-sized pores.

Mineralogy and petrology exert complex impacts on the pore-scale heterogeneity. Higher rigid grain content is generally favorable for the homogeneity of different-sized pores, with exception the heterogeneity increases of medium-sized pores induced by the increasing fracturing risks and heterogeneity increases of large-sized pores resulted from feldspar dissolution. The effects of carbonate are just in the opposite. Greater clay content reduces the heterogeneity of small-sized pores, increases that of medium-sized pores, but increases that of large-sized pores before 5% and then reduces it. The heterogeneities of large-sized and medium-sized pores are more susceptible to the pore fillings, while that of small-sized pores is more susceptible to the matrix grains. The rigid grain benefits the system homogeneity, while the feldspar, rock fragment, and carbonate are on the contrary. Greater grain size and better sorting bring reductions to the heterogeneity of small-sized pores but increases to those of medium- and large-sized pores. The system heterogeneity is mainly correlated to sorting.

The fluid mobility of tight gas sandstone is varied with accessible saturation in the range 8.37–43.87%, which is predominantly attributed to the fluid accessibility differences in the large-sized and medium-sized pores. These differences are closely associated with the pore-scale heterogeneity. Heterogeneity increases exert different impacts in different-sized pores, which result accessibility losses in the medium-sized and large-sized pores but have poor influences in small-sized pores owing to the extra effects of strong clay hydrophillia.

The Coates model on permeability estimation is improved by reevaluating the FFI/BVI according the fluid accessibilities of different-sized pores, considering the effects of system heterogeneity, and excluding the porosity and permeability outliers. The improvement also suggests that it is necessary to investigate the permeability variation mechanisms from the pore-scale perspective.

This study provides deep understandings for the origins and controls of the pores-scale heterogeneity, and its effects on the fluid accessibility. It may enlighten the associated studies in microscopic structure, fluid flow in tight porous media, and reservoir quality evaluation.

Credit roles

Juncheng Qiao: Conceptualization, Methodology, Software, Investigation, Writing-Original Draft, Resources. **Jianhui Zeng:** Supervision, Writing – Review & Editing, Project administration, Funding acquisition, Resources. **Jianchao Cai:** Investigation. **Shu Jiang:** Investigation. **Ting An:** Investigation. **Enzhao Xiao:** Investigation. **Yongchao Zhang:** Software. **Xiao Feng:** Software. **Guangqing Yang:** Investigation.

Declaration of competing interest

The authors declare that they have no known competing financial interests or personal relationships that could have appeared to influence the work reported in this paper.

Acknowledgements

This study is supported by the National Natural Science Foundation of China (Grant No. 41330319), Foundation of China University of Petroleum Beijing (Grant No. 2462020XKBH016), and fellowship of China Postdoctoral Science Foundation (Grant No. 2020M680030). We sincerely appreciate all anonymous reviewers and the handling editor for their comments and suggestions.

References

Aghaei, A., Piri, M., 2015. Direct pore-to-core up-scaling of displacement processes: dynamic pore network modeling and experimentation. J. Hydrol. 522, 488–509.
Ajdukiewicz, J.M., Lander, R.H., 2010. Sandstone reservoir quality prediction: the state of the art. AAPG Bull. 94 (8), 1083–1091.
Amaefule, J.O., Altunbay, M., Tiab, D., Kersey, D.G., Keelan, D.K., 1993. Enhanced reservoir description: using core and log data to identify hydraulic (flow) units and predict permeability in uncored intervals/wells. In: SPE Annual Technical Conference and Exhibition. Houstan, Texas.
Angulo, R., Alvarado, V., Gonzalez, H., 1992. Fractal dimensions from mercury intrusion capillary tests. In: SPE Latin America Petroleum Engineering Conference. Caracas, Venezuela.
Arns, C.H., Knackstedt, M.A., Martys, N.S., 2005. Cross-property correlations and permeability estimation in sandstone. Phys. Rev. E 72, 046304.
Arns, C.H., Knackstedt, M.A., Pinczewski, M.V., Lindquist, W., 2001. Accurate estimation of transport properties from microtomographic images. Geophys. Res. Lett. 28, 3361–3364.
Arshadi, M., Khishvand, M., Aghaei, A., Piri, M., Al-Muntasheri, G., 2018. Pore-scale experimental investigation of two-phase flow through fractured porous media. Water Resour. Res. 54, 3602–3631.
Bahadur, J., Melnichenko, Y., Mastalerz, M., Furmann, A., Clarkson, C.R., 2014. Hierarchical pore morphology of cretaceous shale: a small-angle neutron scattering and ultrasmall-angle neutron scattering study. Energy Fuels 28 (10), 6336–6344.
Bale, H.D., Schmidt, P.W., 1984. Small-angle X-ray-scattering investigation of submicroscopic porosity with fractal properties. Phys. Rev. Lett. 53 (6), 596.
Bear, J., 2013. Dynamics of fluids in porous media. Dover Publications Inc, NewYork.
Bjørlykke, K., Ramm, M., Saigal, G.C., 1989. Sandstone diagenesis and porosity modification during basin evolution. Geol. Rundsch. 78 (1), 243–268.
Blunt, M.J., 1998. Physically-based network modeling of multiphase flow in intermediate-wet porous media. J. Petrol. Sci. Eng. 20, 117–125.
Boggs Jr., S., Boggs, S., 2009. Petrology of sedimentary rocks. Macmillan Publishing Company, New York.
Bourbie, T., Zinszner, B., 1985. Hydraulic and acoustic properties as a function of porosity in Fontainebleau sandstone. J. Geophys. Res.: Solid Earth 90, 11524–11532.
Cai, J., Luo, L., Ye, R., Zeng, X., Hu, X., 2015. Recent advances on fractal modeling of permeability for fibrous porous media. Fractals 23 (1), 1540006.
Clarkson, C.R., Freeman, M., He, L., Agamalian, M., Melnichenko, Y., Mastalerz, M., Bustin, R., Radliński, A., Blach, T., 2012b. Characterization of tight gas reservoir pore structure using USANS/SANS and gas adsorption analysis. Fuel 95, 371–385.

Clarkson, C.R., Solano, N., Bustin, R.M., Bustin, A., Chalmers, G., He, L., Melnichenko, Y. B., Radliński, A., Blach, T.P., 2013. Pore structure characterization of North American shale gas reservoirs using USANS/SANS, gas adsorption, and mercury intrusion. Fuel 103, 606–616.

Clarkson, C.R., Wood, J., Burgis, S., Aquino, S., Freeman, M., 2012a. Nanopore-structure analysis and permeability predictions for a tight gas siltstone reservoir by use of low-pressure adsorption and mercury-intrusion techniques. SPE Reservoir Eval. Eng. 15 (6), 648–661.

Coates, G., Peveraro, R., Hardwick, A., Roberts, D., 1991. The Magnetic Resonance Imaging Log Characterized by Comparison with Petrophysical Properties and Laboratory Core Data. In: SPE Annual Technical Conference and Exhibition. Dallas, Texas.

Daigle, H., Dugan, B., 2009. Extending NMR data for permeability estimation in fine-grained sediments. Mar. Petrol. Geol. 26, 1419–1427.

Daigle, H., Johnson, A., Thomas, B., 2014a. Determining fractal dimension from nuclear magnetic resonance data in rocks with internal magnetic field gradients. Geophysics 79 (6), D425–D431.

Daigle, H., Johnson, A., 2016. Combining mercury intrusion and nuclear magnetic resonance measurements using percolation theory. Transp. Porous Media 111, 669–679.

Daigle, H., Thomas, B., Rowe, H., Nieto, M., 2014b. Nuclear magnetic resonance characterization of shallow marine sediments from the nankai trough, integrated ocean drilling program expedition 333. J. Geophys. Res.: Solid Earth 119 (4), 2631–2650.

Desbois, G., Urai, J.L., Kukla, P.A., Konstanty, J., Baerle, C., 2011. High-resolution 3D fabric and porosity model in a tight gas sandstone reservoir: a new approach to investigate microstructures from mm-to nm-scale combining argon beam cross-sectioning and SEM imaging. J. Petrol. Sci. Eng. 78 (2), 243–257.

Dillinger, A., Esteban, L., 2014. Experimental evaluation of reservoir quality in Mesozoic formations of the Perth Basin (Western Australia) by using a laboratory low field Nuclear Magnetic Resonance. Mar. Petrol. Geol. 57, 455–469.

Dong, H., Blunt, M.J., 2009. Pore-network extraction from micro-computerized-tomography images. Phys. Rev. E 80 (3), 036307.

Dou, W., Liu, L., Wu, K., Xu, Z., Liu, X., Feng, X., 2018. Diagenetic heterogeneity, pore throats characteristic and their effects on reservoir quality of the Upper Triassic tight sandstones of Yanchang Formation in Ordos Basin, China. Mar. Petrol. Geol. 98, 243–257.

Dullien, F.A., 2012. Porous media: Fluid transport and pore structure. Academic press, San Diego.

Friesen, W., Mikula, R., 1987. Fractal dimensions of coal particles. J. Colloid Interface Sci. 120 (1), 263–271.

Fu, H., Tang, D., Xu, T., Xu, H., Tao, S., Li, S., Yin, Z., Chen, B., Zhang, C., Wang, L., 2017. Characteristics of pore structure and fractal dimension of low-rank coal: a case study of Lower Jurassic Xishanyao coal in the southern Junggar Basin, NW China. Fuel 193, 254–264.

Gallegos, D.P., Munn, K., Smith, D.M., Stermer, D.L., 1987. A NMR technique for the analysis of pore structure: application to materials with well-defined pore structure. J. Colloid Interface Sci. 119, 127–140.

Gao, H., Li, H.A., 2016. Pore structure characterization, permeability evaluation and enhanced gas recovery techniques of tight gas sandstones. J. Nat. Gas Sci. Eng. 28, 536–547.

Ge, X., Fan, Y., Deng, S., Han, Y., Liu, J., 2016. An improvement of the fractal theory and its application in pore structure evaluation and permeability estimation. J. Geophys. Res.: Solid Earth 121 (9), 6333–6345.

Ge, X., Fan, Y., Zhu, X., Chen, Y., Li, R., 2015. Determination of nuclear magnetic resonance T_2 cutoff value based on multifractal theory—an application in sandstone with complex pore structure. Geophysics 80 (1), D11–D21.

Giles, M.R., Marshall, J.D., 1986. Constraints on the development of secondary porosity in the subsurface: re-evaluation of processes. Mar. Petrol. Geol. 3 (3), 243–255.

Hansen, J., Skjeltorp, A., 1988. Fractal pore space and rock permeability implications. Phys. Rev. B 38 (4), 2635.

Holditch, S.A., 2006. Tight gas sands. J. Petrol. Technol. 58 (6), 86–93.

Huang, S., Wu, Y., Meng, X., Liu, L., Ji, W., 2018. Recent advances on microscopic pore characteristics of low permeability sandstone reservoirs. Adv. Geo-Energy Res. 2 (2), 122–134.

Jiang, F., Chen, D., Chen, J., Li, Q., Liu, Y., Shao, X., Hu, T., Dai, J., 2016. Fractal analysis of shale pore structure of continental gas shale reservoir in the Ordos Basin, NW China. Energy Fuels 30 (6), 4676–4689.

Katsube, T., Williamson, M., 1994. Effects of diagenesis on shale nano-pore structure and implications for sealing capacity. Clay Miner. 29 (4), 451–461.

Katz, A., Thompson, A., 1986. Quantitative prediction of permeability in porous rock. Phys. Rev. B 34 (11), 8179.

Katz, A.J., Thompson, A., 1985. Fractal sandstone pores: implications for conductivity and pore formation. Phys. Rev. Lett. 54 (12), 1325.

Krohn, C., Thompson, A., 1986. Fractal sandstone pores: automated measurements using scanning-electron-microscope images. Phys. Rev. B 33 (9), 6366.

Krohn, C.E., 1988. Fractal measurements of sandstones, shales, and carbonates. J. Geophys. Res.: Solid Earth 93 (B4), 3297–3305.

Lai, J., Wang, G., 2015. Fractal analysis of tight gas sandstones using high-pressure mercury intrusion techniques. J. Nat. Gas Sci. Eng. 24, 185–196.

Lai, J., Wang, G., Fan, Z., Zhou, Z., Chen, J., Wang, S., 2018a. Fractal analysis of tight shaly sandstones using nuclear magnetic resonance measurements. AAPG Bull. 102 (2), 175–193.

Lai, J., Wang, G., Wang, Z., Chen, J., Pang, X., Wang, S., Zhou, Z., He, Z., Qin, Z., Fan, X., 2018b. A review on pore structure characterization in tight sandstones. Earth Sci. Rev. 177, 436–457.

Lai, J., Wang, G.W., Chai, Y., Ran, Y., Zhang, X., 2015. Depositional and diagenetic controls on pore structure of tight gas sandstone reservoirs: evidence from lower cretaceous bashijiqike Formation in kelasu thrust belts, kuqa depression in tarim basin of west China. Resour. Geol. 65 (2), 55–75.

Li, K., 2010. Analytical derivation of Brooks–Corey type capillary pressure models using fractal geometry and evaluation of rock heterogeneity. J. Petrol. Sci. Eng. 73 (1–2), 20–26.

Li, K., Horne, R.N., 2006. Fractal modeling of capillary pressure curves for the Geysers rocks. Geothermics 35 (2), 198–207.

Li, P., Zheng, M., Bi, H., Wu, S., Wang, X., 2017. Pore throat structure and fractal characteristics of tight oil sandstone: a case study in the Ordos Basin, China. J. Petrol. Sci. Eng. 149, 665–674.

Liu, H., Zhu, Z., Patrick, W., Liu, J., Lei, H., Zhang, L., 2020. Pore-scale numerical simulation of supercritical CO_2 migration in porous and fractured media saturated with water. Adv. Geo-Energy Res. 4 (4), 419–434.

Liu, M., Xie, R., Guo, J., Jin, G., 2018. Characterization of pore structures of tight sandstone reservoirs by multifractal analysis of the NMR T 2 distribution. Energy Fuels 32 (12), 12218–12230.

Liu, X., Xiong, J., Liang, L., 2015. Investigation of pore structure and fractal characteristics of organic-rich Yanchang formation shale in central China by nitrogen adsorption/desorption analysis. J. Nat. Gas Sci. Eng. 22, 62–72.

Mandelbrot, B.B., 1975. Les objets fractals: forme, hasard et dimension. Flammarion, Paris.

Mandelbrot, B.B., Passoja, D.E., Paullay, A.J., 1984. Fractal character of fracture surfaces of metals. Nature 308 (5961), 721–722.

McKinley, J., Atkinson, P.M., Lloyd, C.D., Ruffell, A.H., Worden, R., 2011. How porosity and permeability vary spatially with grain size, sorting, cement volume, and mineral dissolution in fluvial Triassic sandstones: the value of geostatistics and local regression. J. Sediment. Res. 81 (12), 844–858.

Mozley, P.S., Heath, J.E., Dewers, T.A., Bauer, S.J., 2016. Origin and heterogeneity of pore sizes in the mount simon sandstone and eau claire formation: implications for multiphase fluid flow. Geosphere 12 (4), 1341–1361.

Pape, H., Clauser, C., Iffland, J., 1999. Permeability prediction based on fractal pore-space geometry. Geophysics 64, 1447–1460.

Pan, J., Wang, K., Hou, Q., Niu, Q., Wang, H., Ji, Z., 2016. Micro-pores and fractures of coals analysed by field emission scanning electron microscopy and fractal theory. Fuel 164, 277–285.

Peng, R., Yang, Y., Ju, Y., Mao, L., Yang, Y., 2011. Computation of fractal dimension of rock pores based on gray CT images. Chin. Sci. Bull. 56 (31), 3346–3357.

Peyton, R.L., Gantzer, C.J., Anderson, S.H., Haeffner, B.A., Pfeifer, P., 1994. Fractal dimension to describe soil macropore structure using X ray computed tomography. Water Resour. Res. 30 (3), 691–700.

Qiao, J., Zeng, J., Jiang, S., Ma, Y., Feng, S., Xie, H., Wang, Y., Hu, H., 2020a. Role of pore structure in the percolation and storage capacities of deeply buried sandstone reservoirs: a case study of the Junggar Basin. China. Mar. Petrol. Geol. 113, 104129.

Qiao, J., Zeng, J., Jiang, S., Wang, Y., 2020b. Impacts of sedimentology and diagenesis on pore structure and reservoir quality in tight oil sandstone reservoirs: implications for macroscopic and microscopic heterogeneities. Mar. Petrol. Geol. 111, 279–300.

Qiao, J., Zeng, J., Jiang, S., Zhang, Y., Feng, S., Feng, X., Hu, H., 2020c. Insights into the pore structure and implications for fluid flow capacity of tight gas sandstone: a case study in the upper paleozoic of the Ordos Basin. Mar. Petrol. Geol. 104439.

Qiao, J., Zeng, J., Feng, X., Yang, Z., Zhang, Y., Feng, S., 2017. Characteristics of nano-nicro pore networks and petroleum microscopic occurrence state in ultra-low permeability (tight) sandstone reservoir. J. Nanosci. Nanotechnol. 17 (9), 6039–6050.

Radlinski, A., Ioannidis, M., Hinde, A., Hainbuchner, M., Baron, M., Rauch, H., Kline, S., 2004. Angstrom-to-millimeter characterization of sedimentary rock microstructure. J. Colloid Interface Sci. 274 (2), 607–612.

Rahner, M.S., Halisch, M., Fernandes, C.P., Weller, A., dos Santos, V.S.S., 2018. Fractal dimensions of pore spaces in unconventional reservoir rocks using X-ray nano-and micro-computed tomography. J. Nat. Gas Sci. Eng. 55, 298–311.

Rezaee, R., Saeedi, A., Clennell, B., 2012. Tight gas sands permeability estimation from mercury injection capillary pressure and nuclear magnetic resonance data. J. Petrol. Sci. Eng. 88, 92–99.

Sahimi, M., 1993. Flow phenomena in rocks: from continuum models to fractals, percolation, cellular automata, and simulated annealing. Rev. Mod. Phys. 65 (4), 1393–1534.

Soeder, D., 1984. Reservoir properties and pore structure of tight gas sands. AAPG Bull. 68 (4), 530-530.

Soeder, D.J., Chowdiah, P., 1990. Pore geometry in high-and low-permeability sandstones, travis peak formation, east Texas. SPE Form. Eval. 5 (4), 421–430.

Song, Z., Liu, G., Yang, W., Zou, H., Sun, M., Wang, X., 2018. Multi-fractal distribution analysis for pore structure characterization of tight sandstone—a case study of the Upper Paleozoic tight formations in the Longdong District, Ordos Basin. Mar. Petrol. Geol. 92, 842–854.

Sun, M., Yu, B., Hu, Q., Zhang, Y., Li, B., Yang, R., Melnichenko, Y.B., Cheng, G., 2017. Pore characteristics of Longmaxi shale gas reservoir in the Northwest of Guizhou, China: investigations using small-angle neutron scattering (SANS), helium pycnometry, and gas sorption isotherm. Int. J. Coal Geol. 171, 61–68.

Tang, X., Zhang, J., Shan, Y., Xiong, J., 2012. Upper Paleozoic coal measures and unconventional natural gas systems of the Ordos Basin, China. Geosci. Front. 3 (6), 863–873.

Tiab, D., Donaldson, E.C., 2004. Petrophysics: Theory and Practice of Measuring Reservoir Rock and Fluid Transport Properties. Gulf professional publishing.

Tsakiroglou, C.D., Payatakes, A.C., 2000. Characterization of the pore structure of reservoir rocks with the aid of serial sectioning analysis, mercury porosimetry and network simulation. Adv. Water Resour. 23 (7), 773–789.
Wang, H., Liu, Y., Song, Y., Zhao, Y., Zhao, J., Wang, D., 2012. Fractal analysis and its impact factors on pore structure of artificial cores based on the images obtained using magnetic resonance imaging. J. Appl. Geophys. 86, 70–81.
Wang, Z., Li, H., Lan, X., Wang, K., Yang, Y., Lisitsa, V., 2021. Formation damage mechanism of a sandstone reservoir based on micro-computed tomography. Adv. Geo-Energy Res. 5 (1), 25–38.
Wang, Z., Pan, M., Shi, Y., Liu, L., Xiong, F., Qin, Z., 2018. Fractal analysis of Donghetang sandstones using NMR measurements. Energy Fuels 32 (3), 2973–2982.
Wilson, L., Wilson, M., Green, J., Patey, I., 2014. The influence of clay mineralogy on formation damage in North Sea reservoir sandstones: a review with illustrative examples. Earth Sci. Rev. 134, 70–80.
Wu, Y., Tahmasebi, P., Lin, C., Zahid, M.A., Dong, C., Golab, A.N., Ren, L., 2019. A comprehensive study on geometric, topological and fractal characterizations of pore systems in low-permeability reservoirs based on SEM, MICP, NMR, and X-ray CT experiments. Mar. Petrol. Geol. 103, 12–28.
Xia, Y., Cai, J., Perfect, E., Wei, W., Zhang, Q., Meng, Q., 2019. Fractal dimension, lacunarity and succolarity analyses on CT images of reservoir rocks for permeability prediction. J. Hydrol. 579, 124198.
Xiao, L., Liu, D., Wang, H., Li, J., Lu, J., Zou, C., 2017. The applicability analysis of models for permeability prediction using mercury injection capillary pressure (MICP) data. J. Petrol. Sci. Eng. 156, 589–593.
Xiao, X., Zhao, B., Thu, Z., Song, Z., Wilkins, R., 2005. Upper paleozoic petroleum system, Ordos basin, China. Mar. Petrol. Geol. 22 (8), 945–963.
Yang, F., Ning, Z., Liu, H., 2014. Fractal characteristics of shales from a shale gas reservoir in the Sichuan Basin, China. Fuel 115, 378–384.
Yang, H., Fu, J., Liu, X., Meng, P., 2012. Accumulation conditions and exploration and development of tight gas in the Upper Paleozoic of the Ordos Basin. Petrol. Explor. Dev. 39 (3), 315–324.
Yang, H., Fu, J., Wei, X., Liu, X., 2008. Sulige field in the Ordos Basin: geological setting, field discovery and tight gas reservoirs. Mar. Petrol. Geol. 25 (4–5), 387–400.
Yang, R., He, S., Yi, J., Hu, Q., 2016. Nano-scale pore structure and fractal dimension of organic-rich Wufeng-Longmaxi shale from Jiaoshiba area, Sichuan Basin: investigations using FE-SEM, gas adsorption and helium pycnometry. Mar. Petrol. Geol. 70, 27–45.
Yao, Y., Liu, D., Tang, D., Tang, S., Huang, W., 2008. Fractal characterization of adsorption-pores of coals from North China: an investigation on CH_4 adsorption capacity of coals. Int. J. Coal Geol. 73 (1), 27–42.
Yuan, Y., Rezaee, R., 2019. Fractal analysis of the pore structure for clay bound water and potential gas storage in shales based on NMR and N_2 gas adsorption. J. Petrol. Sci. Eng. 177, 756–765.
Zhang, C., Chen, Z., Zhang, Z., Li, J., Ling, H., Sun, B., 2007. Fractal characteristics of reservoir rock pore structure based on NMR T_2 distribution. J. Oil Gas Technol. 29 (4), 80–86.
Zhang, K., Lai, J., Bai, G., Pang, X., Ma, X., Qin, Z., Zhang, X., Fan, X., 2020. Comparison of fractal models using NMR and CT analysis in low permeability sandstones. Mar. Petrol. Geol. 112, 104069.
Zhao, J., Zhang, W., Li, J., Cao, Q., Fan, Y., 2014. Genesis of tight sand gas in the Ordos Basin. China. Org. Geochem. 74, 76–84.
Zhao, Y., Zhu, G., Dong, Y., Danesh, N.N., Chen, Z., Zhang, T., 2017. Comparison of low-field NMR and microfocus X-ray computed tomography in fractal characterization of pores in artificial cores. Fuel 210, 217–226.
Zheng, S., Yao, Y., Liu, D., Cai, Y., Liu, Y., 2018. Characterizations of full-scale pore size distribution, porosity and permeability of coals: a novel methodology by nuclear magnetic resonance and fractal analysis theory. Int. J. Coal Geol. 196, 148–158.
Zhou, S., Liu, D., Cai, Y., Yao, Y., 2016. Fractal characterization of pore–fracture in low-rank coals using a low-field NMR relaxation method. Fuel 181, 218–226.
Zhu, R., Zou, C., Zhang, N., Wang, X., Cheng, R., Liu, L., Zhou, C., Song, L., 2008. Diagenetic fluids evolution and genetic mechanism of tight sandstone gas reservoirs in Upper Triassic Xujiahe Formation in Sichuan Basin, China. Sci. China Ser. D: Earth Sciences 51 (9), 1340–1353.
Zou, C., Zhu, R., Liu, K., Su, L., Bai, B., Zhang, X., Yuan, X., Wang, J., 2012. Tight gas sandstone reservoirs in China: characteristics and recognition criteria. J. Petrol. Sci. Eng. 88, 82–91.